Geochimica et Cosmochimica Acta 359 (2023) 148–164

Contents lists available at ScienceDirect

Geochimica et Cosmochimica Acta

journal homepage: www.elsevier.com/locate/gca

# Constraining the major pathways of vanadium incorporation into sediments underlying natural sulfidic waters

Minming Cui [a,b,*], George W. Luther III [c], Maya Gomes [a]

[a] Department of Earth and Planetary Sciences, Johns Hopkins University, Baltimore, MD 21218-2687, USA
[b] State Key Laboratory of Environmental Geochemistry, Institute of Geochemistry, Chinese Academy of Sciences, Guiyang 550081, China
[c] School of Marine Science and Policy, University of Delaware, 700 Pilottown Road, Lewes, DE 19958, USA

ARTICLE INFO

*Associate editor:* Natascha Riedinger

*Keywords:*
Vanadium
Manganese
V/Mn molar ratio
Manganese oxides
Pyrite
Sulfide
Redox proxy
Chesapeake Bay

ABSTRACT

Vanadium (V) is a redox-sensitive trace metal. Interconversion between different vanadium species (e.g., $V^{III}$, $V^{IV}$, $V^{V}$) occurs rapidly in association with changes in redox conditions in natural environments. Different vanadium species exhibit variable geochemical behavior that impacts if and how they are sequestered into sediments, which makes vanadium a useful proxy for ancient ocean redox conditions. However, we still lack constraints on how different dissolved vanadium sink pathways impact distributions of vanadium in water column, pore waters, and sediments, especially in natural sulfidic settings. In the present study, we combined field and experimental data to constrain the major scavenging processes that influence the partitioning of vanadium between aqueous and solid phases to provide an improved picture of vanadium geochemical cycling under anoxic-sulfidic conditions. We find that in the sulfidic bottom waters and sediment pore waters of the Chesapeake Bay, vanadium concentrations are correlated with manganese (Mn) concentrations in both aqueous and solid phases. Our experimental results support our interpretation that elevated concentrations of vanadium in anoxic-sulfidic waters result from the release of vanadium due to desorption from and/or dissolution of Mn oxides in anoxic/sulfidic waters. While sorption of vanadium results in strongly adsorbed complexes on both Mn oxides and pyrite surfaces, vanadium preferentially sorbs to Mn oxides rather than to pyrite. Thus, the impact of Mn oxides on vanadium geochemistry is greater than that imposed by scavenging via sorption on pyrite, although both processes should be considered. Mn oxides also have a greater impact on vanadium geochemistry than reductive formation of solid $V(OH)_3$ by $H_2S$. Sorption of vanadium is sensitive to pH conditions (especially in anoxic waters), moderately sensitive to ionic strength, and weakly sensitive to phosphate concentrations. In addition, our results show that as waters become more sulfidic, dissolved V/Mn molar ratios increase, whereas solid phase V/Mn molar ratios decrease, indicating that the V/Mn molar ratio can be used to trace redox changes. Finally, we investigate the V/Mn record of black shales that span the Proterozoic and Phanerozoic to show a framework of utilizing this proxy with applicability to identify changes in redox conditions associated with both oxygenation and anoxic events in ancient oceans.

## 1. Introduction

To better understand the Earth-life coevolution, researchers have developed a comprehensive toolbox to reconstruct ancient ocean redox conditions. The toolbox includes redox-sensitive trace metals, which are widely used as paleoredox proxies (Brumsack, 2006; Tribovillard et al., 2006; Scott et al., 2008; Owens et al., 2012; Large et al., 2014; Lyons et al., 2014). Over the past decades, many investigations have focused on modern aquatic environments to better understand the geochemical behaviors of redox-sensitive trace metals and relationships with iron, manganese, sulfur, and organic carbon cycling during early diagenetic processes (e.g., Huerta-Diaz and Morse, 1992; Morford and Emerson, 1999; Chappaz et al., 2008; Olson et al., 2017; Dellwig et al., 2019; Bennett and Canfield, 2020). These modern investigations allow us to place constraints on the mechanisms of sequestration of redox-sensitive trace metals into sediments and thus improve the applicability of the redox proxy toolbox.

Among the redox-sensitive trace metals, vanadium (V) is of interest because it can exist in various oxidation states (e.g., $V^{III}$, $V^{IV}$, $V^{V}$) that range in particle reactivity in natural environments depending on redox

* Corresponding author.
*E-mail address:* mcui5@jhu.edu (M. Cui).

https://doi.org/10.1016/j.gca.2023.08.008
Received 21 July 2022; Accepted 4 August 2023
Available online 7 August 2023

conditions (Wanty and Goldhaber, 1992; Gustafsson, 2019). However, uncertainty remains about how different dissolved vanadium sink pathways are linked to the distributions of V in water column, pore waters, and associated aquatic sediments in natural anoxic-sulfidic waters.

In oxic seawater, vanadium predominantly occurs in the +5 oxidation state ($V^V$) as the highly soluble vanadate oxyanion (e.g., $H_2V^VO_4^-$, $HV^VO_4^{2-}$; Wanty and Goldhaber, 1992; Gustafsson, 2019). Vanadium has a residence time between ~$5 \times 10^4$ and ~$13 \times 10^4$ yrs in the modern ocean (Collier, 1984; Jeandel et al., 1987; Schlesinger et al., 2017) and typically displays a nutrient–type profile with values ranging between ~0.03 and ~0.045 μM in the open ocean (Collier, 1984; Jeandel et al., 1987). In addition to being affected by biological uptake and release, vanadium patterns are also impacted by sorption to mineral surfaces. Vanadium can adsorb to Fe-Mn (oxyhydr)oxide and clay minerals (e.g., Peacock and Sherman, 2004; Larsson et al., 2017a,b; Zhu et al., 2018). Specifically, sorption of vanadium on oxide minerals leads to the formation of different inner-sphere complexes (Wehrli and Stumm, 1989; Peacock and Sherman, 2004; Larsson et al., 2017b; Brinza et al., 2019). In addition, sorption of vanadium on oxide mineral surfaces can involve the oxidation of vanadium from the reduced form ($V^{IV}$) to the oxidized form ($V^V$; Larsson et al., 2017b).

In anoxic waters, $V^V$ is favorably reduced to $V^{IV}$ or $V^{III}$, both of which are thermodynamically stable under anoxic and acidic conditions. The reduction of $V^V$ to $V^{IV}$ via sorption of $V^V$ on $Fe^{II}$–bearing minerals may lead to scavenging of vanadium from the water column (White and Peterson, 1996; Carpentier et al., 2003; Ortiz-Bernad et al., 2004; Coker et al., 2020; Vessey and Lindsay, 2020; O'Loughlin et al., 2021). The formation of $V^{III}$ can be followed by the precipitation of $V^{III}$ oxyhydroxides ($V^{III}(OH)_3$; Breit and Wanty, 1991; Wanty and Goldhaber, 1992). Thus, compared to the oxidized forms ($V^{IV}$ or $V^V$), $V^{III}$ is relatively insoluble (Wanty and Goldhaber, 1992; Huang et al., 2015; Gustafsson, 2019). Vanadium scavenging via incorporation into sediment has been observed in coastal anoxic waters (Emerson and Huested, 1991; Shiller and Mao, 1999; Beck et al., 2010; Reckhardt et al., 2017; Whitmore et al., 2019). Although $V^{IV}$ sulfides were found in the Alum Shale (Bian et al., 2022), studies indicate that aqueous thioanions of vanadium only occur at pH > 10 (Müller et al., 1969; Ranade et al., 1970), which limits the formation of $V^{IV}$-S in natural sulfidic waters. It has thus been suggested that high vanadium abundances in black shales are a result of vanadium reduction and sequestration in the sediment under highly reducing conditions, possibly promoted by high $H_2S$ concentrations (Tribovillard et al., 2006; Scott et al., 2017). However, it has been noted that vanadium enrichments are greater in oxygen minimum zone sediments than in sediments deposited under anoxic and sulfidic water columns (Bennett and Canfield, 2020), which highlights the need to better constrain geochemical processes that impact vanadium burial in sediment.

There is also uncertainty about the role of $V^{III}$ in enrichment pathways of vanadium in sediments. It has been suggested that $V^{III}$ can be an important vanadium species in black shales based on the observation that K-edge absorption spectra peaks for vanadium were nearly identical to those of roscoelite (i.e., alumino-silicate containing V) (Wong et al., 1984) in an Ediacaran organic-rich black shale (Sahoo, 2015). However, $V^{III}$ only substitutes a small fraction (~17%) of $Al^{3+}$ in Roscoelite (Heinrich and Levinson, 1955; Wong et al., 1984). Bennett et al. (2018) studied vanadium speciation in modern marine sediments and found that the average oxidation state of vanadium in anoxic sediments was ~3.5, implying a mixture of $V^{III}$ and $V^{IV}$. Thus, it is not clear if vanadium distributions in anoxic environments are dominantly controlled by direct reduction processes or indirect reduction processes via sorption. Thus, additional information about vanadium enrichment pathways will improve our understanding of vanadium burial in anoxic waters. In sum, vanadium speciation and its partitioning into aqueous versus solid phases is impacted by aqueous chemistry (e.g., pH, reducing condition) as well as sorption on different minerals (e.g., reduced vs oxidized). Additional constraints on these processes will improve our ability to use V geochemistry to study ancient ocean redox conditions.

Here we investigate the geochemical behavior of vanadium in natural redox stratified waters using observations and laboratory experiments to link sink pathways of dissolved vanadium to its geochemical cycling in aquatic environments. We investigated the distribution patterns of vanadium in water column, pore waters, and sediments at a seasonally anoxic site in the Chesapeake Bay, which is along the east coast of North America. Seasonal anoxia occurs at the mid-bay region bottom waters of the Chesapeake Bay (Cooper and Brush, 1991; Cornwell and Sampou, 1995). Active manganese redox cycling leads to the accumulation of solid Mn oxides at the anoxic–oxic boundary, and the reductive dissolution of Mn oxide particles results in soluble Mn(II/III) in the anoxic water column (Tebo et al., 1991; Dollhopf et al., 2000; Oldham et al., 2015, 2017). In the sediment, sulfide formed by microbial sulfate reduction can react with iron to form pyrite or other iron sulfide minerals (like mackinawite and greigite) or diffuse into the overlying bottom waters (Roden and Tuttle, 1992; Cornwell and Sampou, 1995). Hence, it is an excellent location to evaluate the impact of Mn oxides on vanadium partitioning into aqueous and solid phases, the scavenging of vanadium via sorption on pyrite, and vanadium reduction to $V(OH)_3$ by $H_2S$. In addition to documenting vanadium geochemistry, we performed kinetic, batch sorption, and sorption envelope experiments to compare scavenging pathways for vanadium under different redox conditions. By comparing different scavenging pathways and linking them to the distributions of vanadium between the aqueous and solid phases, we are able to show how the vanadium/manganese (V/Mn) molar ratio can be used to track changes in redox conditions of ancient oceans.

## 2. Background for study area

On 30 July 2018, we obtained water column samples and sediment cores from the Mid-Bay region of the Chesapeake Bay aboard the R/V *Hugh R. Sharp*. We sampled site 858 with coordinates − 38°58.709N and 76°22.130W with a water depth of ~25 m (Fig. 1). At the time of sampling, the oxic zone extended down to ~19 m in the water column (Hudson et al., 2019). Sulfide was detected at 21 m in the water column and deeper in the water column as well as porewater samples (Cui et al., 2021). This depth of the oxic zone is deeper than is typical at this time of year because of the release of flood waters from the Conowingo Dam (Hudson et al., 2019). The pH was high at the top of the water column (~7.7), and decreased to ~7.2 in the sediment pore waters (Cui et al., 2021). The salinity increased from ~3 near the surface to ~20 ppt in the pore water. This location has abundant iron sulfides as FeS nanoparticles in surface sediment and pyrite throughout the sediment (Cornwell and Sampou, 1995; Anschutz et al., 1998). Additionally, solid $MnO_2$ particles have been found to form at the oxic-anoxic boundary in this location, and their subsequent reduction leads to the release of Mn(II/III) back into solution (Oldham et al., 2015, 2017).

## 3. Methods

### 3.1. Collections of field samples

We followed trace metal sampling procedures outlined in Johannesson et al. (2004). Sampling bottles, vials, bags, and tubes were washed in a series of doubly deionized water (18.2 MΩ cm, Milli-Q water) and $HNO_3$ baths in the lab prior to sampling. We used a pump profiling system on the R/V *Hugh R. Sharp* to collect water column samples for trace metal analyses (Hudson et al., 2019). We preconditioned each sample container three times with sample water. We also prepared sample blanks for all water sampling tasks that followed the approach described in Johannesson et al. (2004), as well as a field blank to ensure that pump tubing did not lead to contamination. Water samples were filtered using a 0.2-μm pore size PVDF filter (Thermo Scientific) and treated with ultrapure $HNO_3$ (Fisher Optima) after collection.

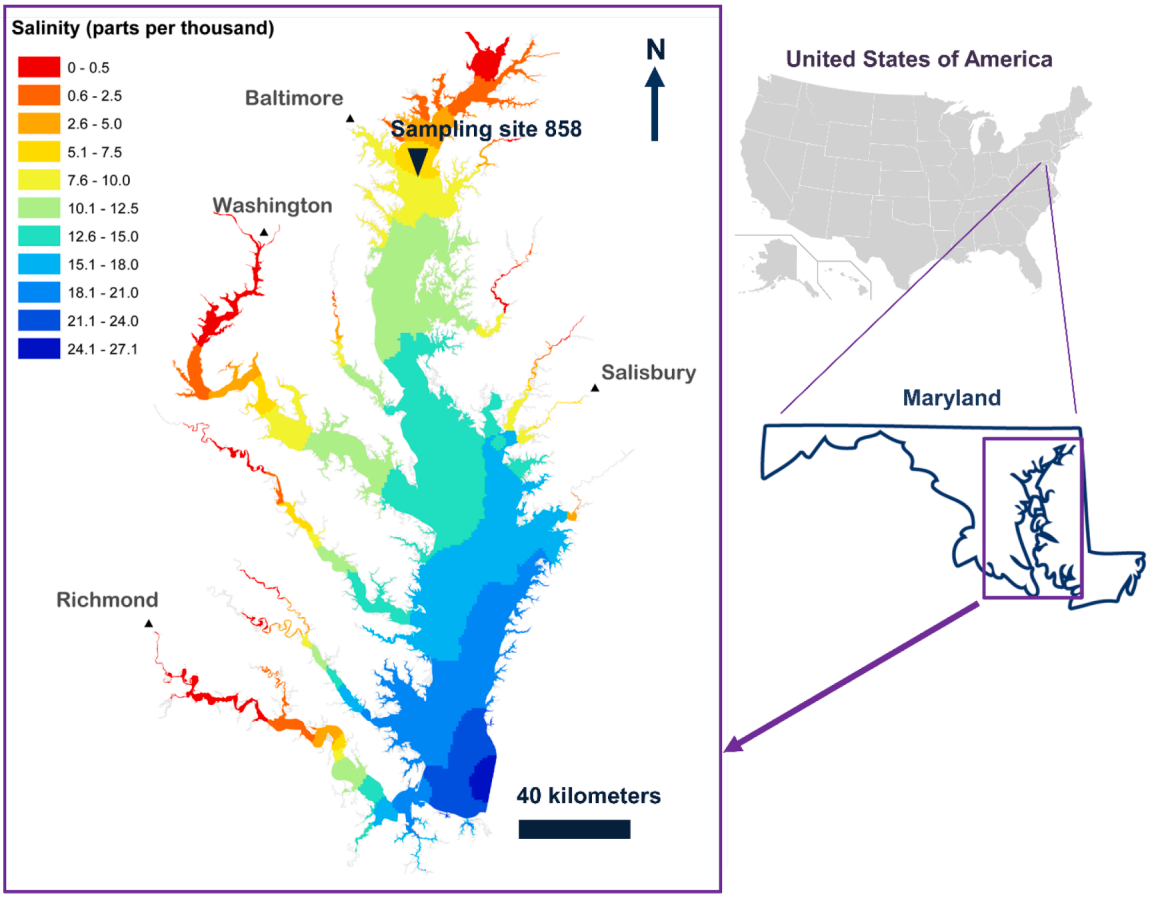


**Fig. 1.** Map of study area showing sample location and salinity gradients. Salinity gradient map is modified from the Chesapeake Bay program (https://www.chesapeakebay.net/what/maps/chesapeake-bay-mean-surface-salinity-1985-2018).

All acidified samples were kept in an ice filled cooler before transferring to the refrigerator at Johns Hopkins University. Sediment cores were collected using a multi-corer with internal diameter of 4 in. Immediately after retrieval, we sectioned the cores into centrifuge tubes (50 mL) in a nitrogen filled glove bag in the wet lab on the ship. The tubes were sealed with parafilm and kept in an ice filled cooler during transport back to the lab and then stored in a refrigerator. Within 2 days, we separated the porewater from the sediment by centrifuging (at 3000 rpm for 1 h). We transferred the pore water samples in a nitrogen-filled glove bag and filtered them using a 0.2-μm pore size PVDF filter (Thermo Scientific). Sediment samples were stored in acid pre-cleaned, dry, capped acrylic tubes following the recommended procedure described in Huerta-Diaz and Morse (1990). These samples were stored at ~4 °C until they were prepared for instrument analysis.

### 3.2. Materials and reagents

We used a $N_2$-filled glove bag to conduct the experiments. All solutions were prepared using doubly deionized water (18.2 MΩ cm, Milli-Q water). Inside the glove bag, the Milli-Q water was bubbled with nitrogen gas (Airgas, Medical NF Grade) for about 30 min. A 5 mM stock solution was prepared for vanadate ($V^V$) by adding sodium metavanadate ($NaV^VO_3$, Aldrich) in the deoxygenated Milli-Q water. Similar to other oxyanion sorption experiments (e.g., Bostick et al., 2003; Cui and Johannesson, 2017), we selected the 3-(N-morpholino) propanesulfonic acid (MOPS) as the pH buffer for $V^V$ sorption experiments. A 100 mM sulfide stock solution was prepared by adding $Na_2S{\cdot}9H_2O$ (Fisher Scientific) to the deoxygenated Milli-Q water. A 10 mM phosphate stock solution was prepared by adding $NaH_2PO_4{\cdot}2H_2O$ (Fisher Scientific) to anoxic Milli-Q water. These stock solutions were stored in the glove bag at room temperature, which is about 25 °C.

Synthetic pyrite was purchased from Strem Chemical (Newburyport, MA, USA). The pyrite is in granular form and has a purity of 95% that is similar to the purity of natural pyrites (~97%; Bonnissel-Gissinger et al., 1998). The surface area of the synthetic pyrite was determined to be ~0.44 $m^2\ g^{-1}$ using nitrogen multi-point BET isotherm (Brunauer et al., 1938), which is within the range of surface areas determined for massive euhedral or nodular from natural settings (0.2–3.1 $m^2\ g^{-1}$; Wolfe et al., 2007). We are unaware of estimates of the framboidal pyrite surface area. Thus, while there may be differences between synthetic and natural pyrites, synthetic pyrite has been widely used for trace metal sorption studies like vanadium, tungsten, and molybdenum (Bostick et al., 2003; Cui and Johannesson, 2017; Vessey and Lindsay, 2020). Pyrite was selected over other iron sulfide minerals because pyrite is the most stable form of iron sulfide minerals under typical marine sediment conditions (Rickard, 2012). Previous studies show that redox sensitive trace metals primarily associate with pyrite in sulfidic marine sediments (Mohajerin, 2014; Cui et al., 2020), and pyrite is the main mineral phase (>90%) in the sulfidic sediments from sites close (~1 km) to our study site in the Chesapeake Bay (Cornwell and Sampou, 1995). Before use, the pyrite was washed with 0.1 M HCl (~30 s) and nitrogen-bubbled Milli-Q water (five times), similar to previously used methods for removal of contaminants from pyrite surfaces (Bostick et al., 2003; Hao et al., 2006). The pretreated pyrite minerals were rinsed with nitrogen-bubbled Milli-Q water and dried overnight and kept in the glove bag at room temperature until use.

Mn-oxide mineral (δ-$MnO_2$) was synthesized using the method described in Foster et al. (2003). We chose δ-$MnO_2$ because it is widely

used for naturally occurring manganese oxide minerals (Fendorf and Zasoski, 1992; Barling and Anbar, 2004). X-ray diffraction patterns of $MnO_2$ (Supplementary Data Fig. S1) were obtained to confirm the purity of the material with a Philips X'Pert PW 3040 Powder diffractometer using Cu Kα radiation. The surface areas were determined to be ~48.32 $m^2$ using nitrogen multi-point BET isotherm (Brunauer et al., 1938).

### 3.3. Adsorption kinetics determination

Experiments for kinetic adsorption of vanadate ($V^V$) were performed to determine the time required for adsorption equilibrium between the dissolved $V^V$ phase and particle associated $V^V$ phase. Kinetic adsorption experiments were performed at room temperature by adding δ-$MnO_2$ (or pyrite) to 20 μM solutions of $V^V$ to attain a concentration of 0.5 g $L^{-1}$ for δ-$MnO_2$ (or 50 g $L^{-1}$ for pyrite) in a 2 mM MOPS buffered solution. All suspensions were prepared in 0.7 M NaCl background electrolyte solutions herein and thereafter in section 3.4 and 3.5. We chose a 100× higher concentration for pyrite because the surface area of δ-$MnO_2$ (~48.32 $m^2$ $g^{-1}$) was ~100× greater than that of pyrite (~0.44 $m^2$ $g^{-1}$). The solution series included two pH conditions: 7.0 ± 0.1 and 8.0 ± 0.1. Initial experiments were run for 48 h to determine sorption equilibrium time, which was 20 h. All subsequent experiments were run for 24 h. At the end of the experiment, the suspension was centrifuged at 3000 rpm for 30 mins to separate the supernatant and suspension. We then filtered the resultant supernatant through a 0.2-μm pore size PVDF filter. The final solution was acidified with the ultrapure $HNO_3$ (Fisher Optima).

Kinetic experiments for $V^V$ scavenging in the presence of $H_2S$ were conducted at room temperature. We added $V^V$ to 1 mM or 2 mM $H_2S$ solutions for a final $V^V$ concentration of 20 μM. The experiments were buffered using 2 mM MOPS solution with a 0.7 M NaCl background electrolyte, adjusted to a pH of 7.0 ± 0.1. At the end of each reaction period, the supernatant and suspension were separated by centrifuging at 3000 rpm for ~30 min. We then filtered the resultant supernatant through a 0.2-μm pore size PVDF filter and applied the same filtering procedure in any following experiment section. The final solution was acidified with the ultrapure $HNO_3$ (Fisher Optima). These solutions were kept at 4 °C before instrument analysis.

### 3.4. Experiments for adsorption isotherm

The $V^V$ was reacted with δ-$MnO_2$ suspensions (0.5 g $L^{-1}$) or pyrite suspensions (50 g $L^{-1}$) at room temperature with $V^V$ concentrations ranging from 0.1 to 200 μM. The experimental solutions included a 0.7 M NaCl background electrolyte. Geochemical modeling of the seawater in this study was achieved using the React program of the Geochemist's Workbench® (Version 12.0.4; Bethke et al., 2018). The stability constants for $V^{III}$ and $V^{IV}$ species are from MINTEQ version 2.4 database, and the stability constants for $V^V$ species are provided in Supplementary Data Table S1. The model predicts activity coefficients for ions other than $Na^+$ and $Cl^-$ up to ionic strengths between 0.5 and 1 M (Zhu and Anderson, 2002; Bethke, 2022), and consequently is able to predict activity coefficients reasonably well for ions in seawater solutions (e.g., Johannesson et al., 2017). Speciation modeling using the stability constants listed in Supplementary Data Table S1 indicates that monomeric vanadate ($H_2V^VO_4^-$ or $HV^VO_4^{2-}$) is the major species at pH > 7 (Supplementary Data Fig. S2). Adsorption experiments were performed at two pH conditions: 7.0 ± 0.1 and 8.0 ± 0.1. After the 24-hour reaction period, the experiment solution was collected, centrifuged, filtered, acidified, and stored as described above.

### 3.5. Experiments for adsorption envelope

The influence of pH on the adsorption of $V^V$ on δ-$MnO_2$ and pyrite surfaces was investigated at room temperature by adding the $V^V$ stock solution to 0.5 g $L^{-1}$ δ-$MnO_2$ or 50 g $L^{-1}$ pyrite suspensions, respectively, to attain a 50 μM concentration of $V^V$. The mineral suspensions were prepared in 0.7 M NaCl background electrolyte solutions. The experimental solutions were adjusted to a pH of ~4 using ultrapure HCl. After a 24-hour period, we measured the equilibrated pH of the experimental solution. The equilibration period of 24 h was determined to be sufficient for attaining equilibrium based on the kinetic experiments (Fig. 4). An aliquot of the experimental suspension was then collected, centrifuged, filtered, acidified, and stored as described above. We continued to sequentially increase the pH of the experimental solution using NaOH until the pH reached ~11, allowing for 24 h of equilibration before sampling as described above. On the same batch, the experiment was also performed in reverse (i.e., from a pH of ~11 to ~4) to study the influence of decreasing pH on $V^V$ adsorption.

### 3.6. Influence of phosphate and ionic strength

The influence of phosphate and ionic strength on vanadium sorption was investigated by adding various concentrations of phosphate (0–150 μM; prepared from $NaH_2PO_4{\cdot}2H_2O$) and $V^V$ simultaneously to 0.5 g $L^{-1}$ δ-$MnO_2$ or 50 g $L^{-1}$ pyrite suspensions to attain a 50 μM $V^V$ at pH = 7.0 ± 0.1. The experiments were performed at NaCl concentrations of 0.001 M and 0.7 M. After the 24-hour reaction period, the experimental solution was collected, centrifuged, filtered, acidified, and stored as described above.

### 3.7. Natural and experimental sample concentration determination

We measured pH using EXTECH Multi-probe DO700 kit, which was calibrated daily with certified pH buffer references at pH 4.0 ± 0.1, 7.0 ± 0.1, and 10.0 ± 0.1. We measured sulfide concentrations of experimental solutions using the methylene blue method (Cline, 1969). Dissolved Mn and sulfide concentrations in natural samples were previously published in Cui et al. (2021). Dissolved vanadium concentrations in natural samples and experiment solutions were quantified using an inductively coupled plasma triple quadrupole mass spectrometry (ICP-QQQ-MS, Agilent 8900) at Johns Hopkins University following procedures described previously (Johannesson et al., 2013; Yang et al., 2015). We prepared a series of vanadium standards using a vanadium standard solution (Vanadium Standard Plasma Grade, Fisher Scientific). Additionally, we routinely analyzed the certified reference material (CRM) for estuarine waters (SLEW-3) purchased from the National Research Council of Canada's (NRC) Metrology Research Center for dissolved V and dissolved Mn to ensure accuracy and analytical uncertainty (Supplementary Data Table S2). The detection limit is 0.01 ppb for dissolved V and dissolved Mn, and 0.2 μM for dissolved sulfide. The determined precision was about 6% or better for five replicate measurements of the CRM SLEW-3 and analytical accuracy of the CRM SLEW-3 was typically within 5% of the values reported by previous studies (e.g., Leonhard et al., 2002; Bayon et al., 2011). About 1–2 g of sediment from each sample were analyzed for solid phase vanadium, manganese, and titanium concentrations via inductively coupled plasma mass spectroscopy by SGS Canada Inc. in Lakefield, Canada. The CRM Ore Research & Exploration Assay Standards (OREAS) 524 and OREAS 135 were routinely analyzed to ensure accuracy and analytical uncertainty (Supplementary Data Table S3). The precision was about 10% or better for two replicate measurements of the CRM OREAS references and analytical accuracy was typically within 15%. The standard error of the measurement replicates was 18% or better and is reported in the Supplementary Data Tables S4–S6.

### 3.8. Geological sedimentary data of vanadium and manganese

We used vanadium and manganese concentration data for black shales from the compiled database of The Sedimentary Geochemistry and Paleoenvironments Project (SGP) (https://sgp.stanford.edu/). We followed the approach described in Farrell et al. (2021) to extract the target data. Briefly, we selected target analytes (geochemical data) from

the SGP database. The data are mainly from: (1) Neoproterozoic and Palaeozoic shales that span globally which were entered by SGP team members, (2) Phanerozoic samples of all lithologies from the United States, which were from the USGS National Geochemical Database, and (3) global shale database spanning all of Earth history which were from the USGS Critical Metals in Black Shales database (Lipp et al., 2021). In total we used vanadium and manganese concentrations in black shales from 12,789 samples with the associated ages. The data used in this study is available in the Supplementary Data.

## 4. Results

### 4.1. Water column and pore water concentrations

Dissolved vanadium concentrations are presented in Fig. 2 along with dissolved Mn and $H_2S$ data from the same sampling period from Cui et al. (2021). Dissolved vanadium concentrations remain stable at ~15.5 nM from 0.5 m to 11 m and decreased to ~11.1 nM with increasing depth in the hypoxic portion of the water column (Hudson et al., 2019). Dissolved Mn concentrations were low (~26.8 nM to ~45.3 nM) in the oxic zone (~0.5 m to ~19 m; Fig. 2b). Below the oxic zone and into the pore waters, both dissolved vanadium and dissolved Mn concentrations increased and reached a maximum of ~551 nM and ~182 μM, respectively (Fig. 2a, b, e, f). There was a peak in pore water for dissolved Mn concentrations of ~114 μM at 3.5 cm, which was characterized by one point (Fig. 2f). Dissolved V/Mn molar ratios decreased from ~1.4 to ~0.24 with increasing water column depth from ~3 m to ~19 m and reached the smallest value of ~0.001 at the sediment water interface (SWI) (Fig. 2c). In pore waters, dissolved V/Mn molar ratios increased and reached a maximum value of ~0.003 (Fig. 2g). Below 20 m water column depth, $H_2S$ became detectable (i.e., >0.2 μM) and increased to a maximum of 11.8 μM in the deepest water column sample (24 m) and continued to increase in the porewaters to ~1200 μM at ~32 cm depth below the surface sediment (Fig. 2d, h).

### 4.2. Solid phase concentrations

Sedimentary vanadium concentrations decreased from ~131 mg $kg^{-1}$ at ~2.5 cm depth in sediments to ~129 mg $kg^{-1}$ at ~31.5 cm depth, but with two peaks defined by single points at ~10 cm depth (~157 mg $kg^{-1}$) and ~20 cm depth (~140 mg $kg^{-1}$), respectively (Fig. 3a). The Mn concentrations increased from ~1004 mg $kg^{-1}$ at ~2.5 cm depth to ~1487 mg $kg^{-1}$ at ~31.5 cm, with two peaks defined by the same single points, at ~10 cm depth (~1533 mg $kg^{-1}$) and ~20 cm depth (~1417 mg $kg^{-1}$), respectively (Fig. 3b). Increases in dissolved vanadium and dissolved manganese with depth in pore waters are in agreement with concentration patterns from Shaw et al. (1994) and from Olson et al. (2017), despite small variations in dissolved vanadium concentrations (~6–28%) and dissolved Mn concentrations (~10–21%) between this study and other studies (Shaw et al., 1994; Olson et al., 2017).

To minimize potential dilution effects by organic matter, opal, and diagenetic minerals, vanadium concentrations were normalized to the immobile element titanium (Ti), which is one of the elements that are mostly unaffected by biological and early diagenetic processes (Brumsack, 2006). We chose Ti over aluminum (Al) because Al may be affected by biogenic fluxes (Murray et al., 1993). The V/Ti ratios increased from ~279 at ~2.5 cm depth to ~315 at ~31.5 cm depth, with two peaks at ~10 cm depth (~349) and ~22 cm depth (~327), respectively (Fig. 3d). In comparison, the Mn/Ti ratios increased from ~2136 at ~2.5 cm depth to ~3627 at ~31.5 cm depth, with two peaks at ~10 cm depth (~3407) and ~22 cm depth (~3472), respectively (Fig. 3e). V/Mn molar ratios decreased with depth in sediments from ~0.13 to a minimum of ~0.087 at ~31.5 cm depth below the SWI (Fig. 3f).

### 4.3. Scavenging kinetics with respect to minerals and sink during reduction by $H_2S$

The results of the kinetic study for $V^V$ adsorption on δ-$MnO_2$ or pyrite are illustrated in Fig. 4. For all cases, we observed a rapid sorption in the

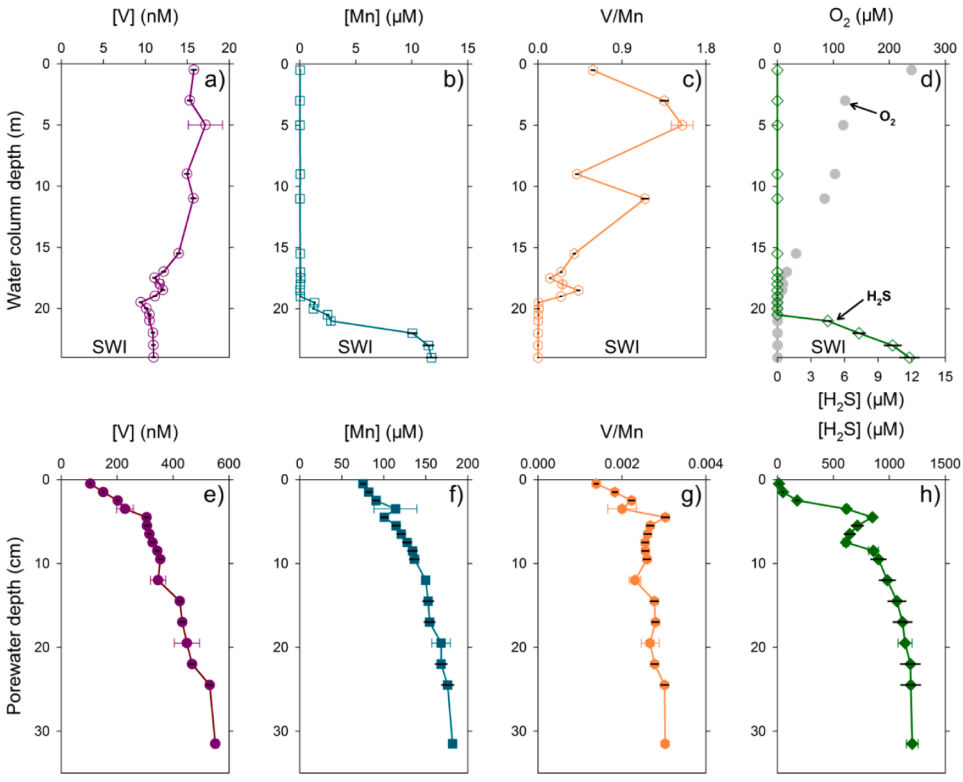


**Fig. 2.** Vertical profiles of dissolved V, dissolved Mn, V/Mn molar ratio, and $H_2S$ in the water column (top) and pore waters (bottom). Water column data are presented as open symbols while solid symbols are used for porewater data. Sediment water interface is abbreviated as SWI. Note that the depth scales differ between the water column (top) and porewater (bottom) and also that the concentration scales for V, Mn, $H_2S$; the V/Mn ratio differs between the top and the bottom. Error bars with any color other than black are equal to one standard deviation (1σ) based on two replicates. Error bars with black color represent the standard error for a single measurement. V/Mn molar ratio (i.e., μM/μM) is unitless. Dissolved Mn and $H_2S$ data are from Cui et al. (2021). Data are provided in Tables S4 and S5 of the Supplementary Data.

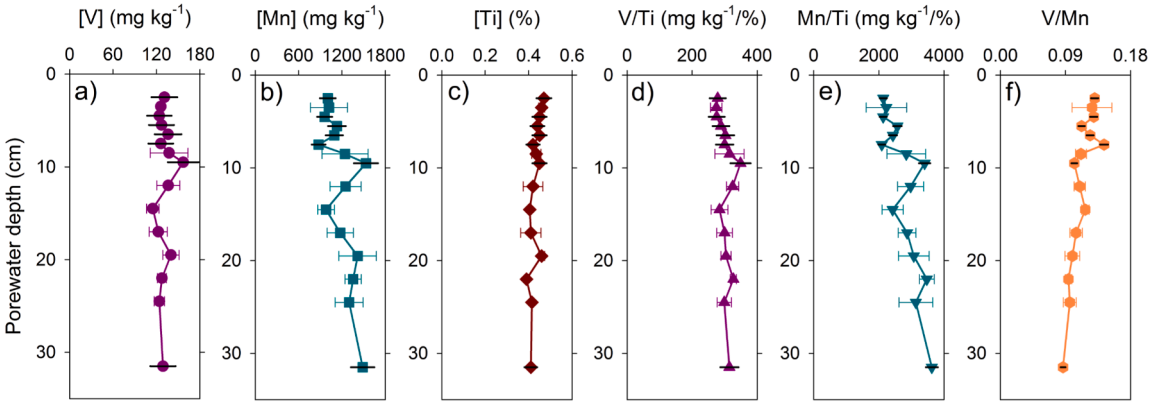


**Fig. 3.** Vertical profiles of solid phase concentrations for (a) V, (b) Mn, (c) Ti, and ratios for (d) V/Ti, (e) Mn/Ti, (f) V/Mn molar ratio. Error bars with any color other than black are equal to one standard deviation (1σ) based on two replicates. Error bars with black color represent the standard error for a single measurement. V/Mn molar ratio (i.e., μM/μM) is unitless. Data are provided in Table S6 of the Supplementary Data.

first 30 min and then the rate of sorption slowed before reaching equilibrium (Fig. 4). For the case of adsorption of $V^V$ on δ-$MnO_2$ at pH 7, there was no further change in the amount of $V^V$ sorbed (~39 μmol $g^{-1}$) with time after 90 min, suggesting that adsorption of $V^V$ on δ-$MnO_2$ had reached equilibrium (Fig. 4a). At pH 8, the amount of $V^V$ sorbed to δ-$MnO_2$ did not increase beyond ~30 μmol $g^{-1}$ after 240 min, suggesting that adsorption of $V^V$ on δ-$MnO_2$ had reached equilibrium (Fig. 4a). For the experiments with pyrite, $V^V$ sorption occurs relatively slowly compared to δ-$MnO_2$ with steady-state partitioning of $V^V$ between pyrite–solution pairs reaching equilibrium after 1200 min for pH 7 and 8 (Fig. 4a, b). The amount of sorbed $V^V$ was greater in experiments with δ-$MnO_2$ (~25–40 μmol $g^{-1}$) than with pyrite (~0.08–0.2 μmol $g^{-1}$).

In comparison to sorption scavenging, $V^V$ sink via reduction in the presence of $H_2S$ and subsequent precipitation to $V(OH)_3$ occurs slower. The induction periods (i.e., the period when no $V^V$ sink occurs) are ~180 min and ~90 min for 1 mM $H_2S$ and 2 mM $H_2S$, respectively (Fig. 4c). After the induction period, the fraction of V sink increased with time (Fig. 4c). At ~2400 min, ~4.4 μmol dissolved $V^V$ per kg water were sunk at 1 mM $H_2S$ and ~6 μmol of the dissolved $V^V$ per kg water were sunk at 2 mM $H_2S$ (Fig. 4c).

### 4.4. Kinetic modeling of vanadium sorption on δ-$MnO_2$ or pyrite

We utilized three kinetic models to estimate the sorption changes for vanadium. These three models include: the pseudo-first-order kinetic model (Lagergren, 1898), (2) the pseudo-second-order kinetic model (Ho and McKay, 1999), and (3) the intraparticle diffusion model (Weber and Morris, 1963). The pseudo-first-order kinetic model followed the equation:

$$\log(q_e - q) = \log(q_e) - \frac{k_1}{2.303}t, \quad (1)$$

The pseudo-second-order kinetic model followed the equation:

$$\frac{t}{q} = \frac{1}{k_{ad}q_e^2} + \frac{1}{q_e}t, \quad (2)$$

in which, the initial sorption rate, $h$ (μmol $g^{-1}$ $min^{-1}$), when t goes to 0 is defined as:

$$h = k_{ad}q_e^2, \quad (3)$$

The intraparticle diffusion model followed the equation:

$$q = k_{id}t^{1/2}. \quad (4)$$

In Eqs. (1)–(4), $q$ (μmol $g^{-1}$) represents the amounts of adsorbed $V^V$ at time $t$ (min), $q_e$ represents the amounts of adsorbed $V^V$ at equilibrium, $k_1$ ($min^{-1}$) is the pseudo-first-order rate constant for $V^V$ adsorption, $k_{ad}$ (g μmol$^{-1}$ $min^{-1}$) is the pseudo-second-order rate constant. In Eq. (4), $k_{id}$ (μmol $g^{-1}$ $min^{-1/2}$) is the rate constant for the intraparticle diffusion model.

The pseudo-second-order model represents the $V^V$ sorption data better than the pseudo-first-order model (Supplementary Data Fig. S3) with the $r^2$ values for the pseudo-second-order model (0.99) being greater than those for the pseudo-first-order model (0.91–0.97). This implies that chemical sorption can better explain the sorption pattern of $V^V$ adsorption on δ-$MnO_2$ and pyrite. The model results also indicate that the initial sorption rate ($h$) for $V^V$ sorption on δ-$MnO_2$ (~1.13–2.51) was ~490–1200 times higher than that (~$0.95 \times 10^{-3}$–$5.12 \times 10^{-3}$) for $V^V$ sorption on pyrite (Table 1). The sorption pattern for the intraparticle diffusion model showed a gradual sorption pattern, and a plateau at equilibrium (Supplementary Data Fig. S3c, f). The rate constant ($k_{id}$) of $V^V$ sorption for intraparticle-diffusion model was estimated from the slope of the first linear portion (Table 1). The estimated $k_{id}$ (~2.39–4.29) for $V^V$ sorption on δ-$MnO_2$ were ~420–770 times greater than those (~$0.31 \times 10^{-2}$–$1.03 \times 10^{-2}$) for $V^V$ sorption on pyrite (Table 1).

### 4.5. Adsorption envelope description

The desorption and sorption curves of $V^V$ on δ-$MnO_2$ or pyrite as a function of pH between pH ~4 and ~11 are illustrated in Fig. 5. The amount of $V^V$ adsorbed on δ-$MnO_2$ or pyrite decreased with increasing pH values. We observed a shift between the desorption and sorption curves for $V^V$ on δ-$MnO_2$ ($p < 0.01$, one-way ANOVA). Both curves are offset at pH 8 to 11 (Fig. 5a). On the other hand, the desorption and sorption curves for $V^V$ on pyrite coalesce at pH 9 to 11 (Fig. 5b). The desorption and sorption curves for $V^V$ on δ-$MnO_2$ or pyrite separate at pH ~5. The irreversible fraction of $V^V$ sorption on δ-$MnO_2$ surface is ~5–14% at pH ~5 to ~8. In comparison, the irreversible fraction of $V^V$ sorption on pyrite is ~4–8%. During the desorption titration, the fraction (~51–72%) of $V^V$ that remains adsorbed on δ-$MnO_2$ at pH ~7–8 is ~2–3 times that of $V^V$ that remains adsorbed on pyrite surfaces (~15–29%; Fig. 5).

### 4.6. Adsorption isotherm description

The sorption processes of $V^V$ on δ-$MnO_2$ or pyrite were characterized using the Freundlich and Langmuir isotherm models. The Freundlich isotherm model (Freundlich, 1906) is commonly used for non-ideal, multilayer adsorption, and is represented by the equation:

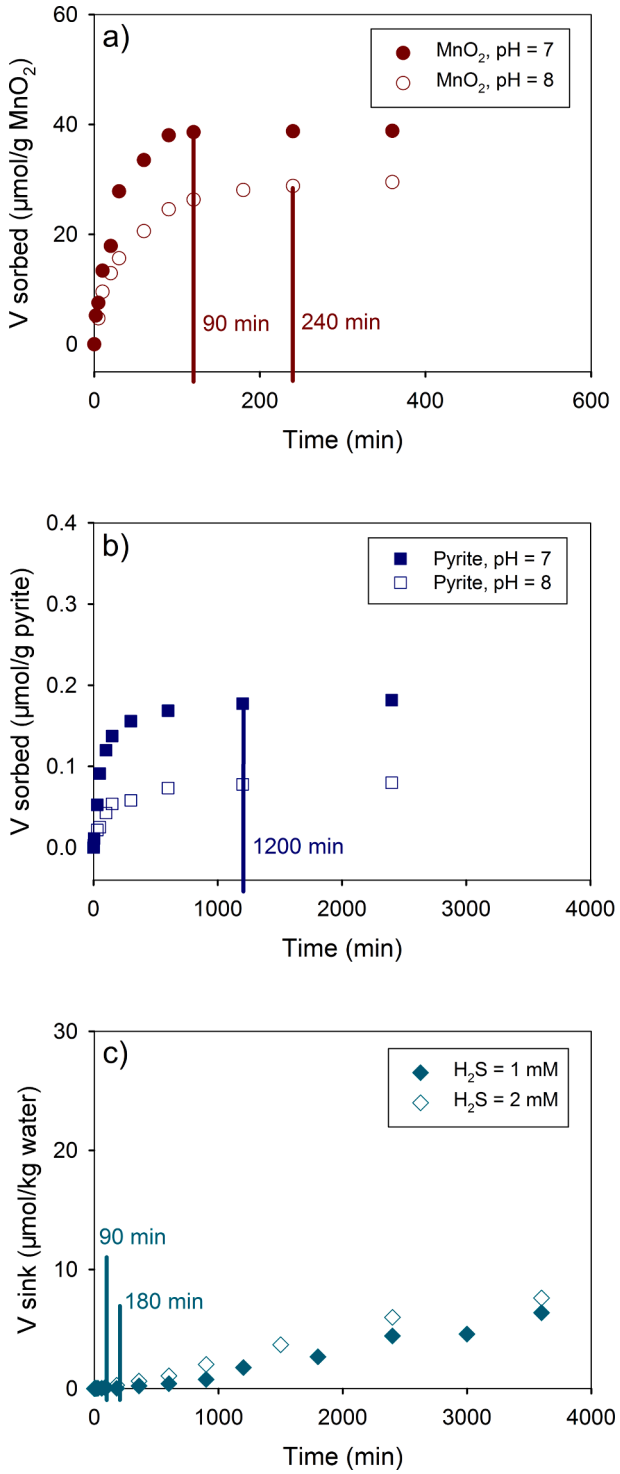


**Fig. 4.** Adsorption of V onto (a) δ-$MnO_2$ and (b) pyrite as a function of contact time at 25 °C, at pH 7 (filled symbols) and 8 (open symbols). And (c) loss of V in the presence of $H_2S$ at 1 mM (filled symbols) and 2 mM (open symbols). The vertical lines for panels (a) and (b) indicate the time that equilibrium is achieved. The vertical lines for panel (c) indicate the induction periods.

$$q_e = K_F C_e^{1/n} \quad (5)$$

in which, $q_e$ (μmol $g^{-1}$) is the amount of $V^V$ adsorbed, $K_F$ (μmol$^{1-n}$ $g^{-1}$ $L^n$) is the distribution coefficient, $C_e$ (μmol $L^{-1}$) is the equilibrium concentration of $V^V$ in solution, and n is a correction factor.

The Langmuir isotherm model (Langmuir, 1918) is valid for single

**Table 1**
Comparison of the pseudo-first-order, pseudo-second-order, and intra-particle diffusion kinetic model rate constants for V adsorbed onto δ-$MnO_2$ and pyrite at pH 7 and 8, respectively.

| | pH | Pseudo-first-order kinetics $k_1$ ($min^{-1}$)[a] | Pseudo-second-order kinetics $h$ (μmol $g^{-1}$ $min^{-1}$)[b] | Pseudo-second-order kinetics $k_{ad}$ (g μmol$^{-1}$ $min^{-1}$)[c] | Intraparticle diffusion kinetics $k_{id}$ (μmol $g^{-1}$ $min^{-1/2}$)[d] |
|---|---|---|---|---|---|
| δ-$MnO_2$ | 7 | $2.78 \times 10^{-2}$ | 2.51 | $1.66 \times 10^{-3}$ | 4.29 |
| | 8 | $1.98 \times 10^{-2}$ | 1.13 | $1.29 \times 10^{-3}$ | 2.39 |
| Pyrite | 7 | $6.21 \times 10^{-3}$ | $5.12 \times 10^{-3}$ | $1.55 \times 10^{-1}$ | $1.03 \times 10^{-2}$ |
| | 8 | $5.98 \times 10^{-3}$ | $0.95 \times 10^{-3}$ | $1.49 \times 10^{-1}$ | $0.31 \times 10^{-2}$ |

[a] $k_1$ ($min^{-1}$) is the pseudo-first-order rate constant.
[b] $h$ (μmol $g^{-1}$ $min^{-1}$) is the pseudo-second-order initial sorption rate.
[c] $k_{ad}$ (g μmol$^{-1}$ $min^{-1}$) is the pseudo-second-order rate constant.
[d] $k_{id}$ (μmol $g^{-1}$ $min^{-1/2}$) is the rate constant for the intraparticle diffusion model.

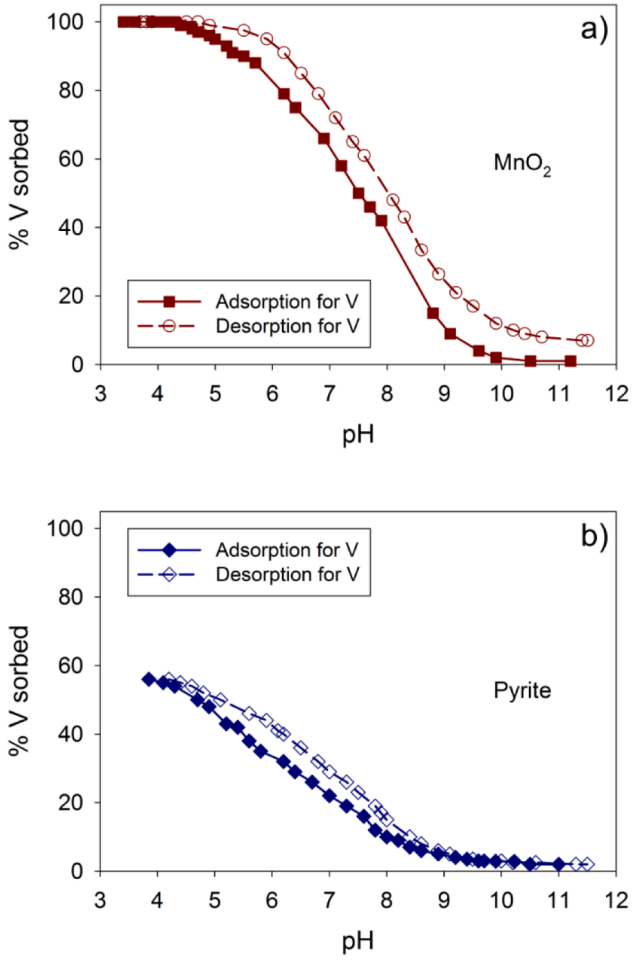


**Fig. 5.** Sorption and desorption of V onto (a) δ-$MnO_2$ and (b) pyrite as a function of decreasing (filled symbols) and increasing (open symbols) pH at 25 °C.

layer adsorption on surfaces containing a finite number of identical sorption sites, and is represented by the equation:

$$q_e = \frac{q_m K_L C_e}{1 + K_L C_e} \quad (6)$$

in which, $q_e$ (μmol $g^{-1}$) is the amount of $V^V$ adsorbed, $q_m$ (μmol $g^{-1}$) is the maximum adsorption capacity, $C_e$ (μmol $L^{-1}$) is the equilibrium concentration of $V^V$ in solution and $K_L$ (L $\mu mol^{-1}$) is the adsorption constant related to the binding energy.

As can be seen from Table 2, the sorption data is better represented by the Langmuir isotherm model compared with the Freundlich isotherm model because $r^2$ values for the Langmuir isotherm model for δ-$MnO_2$ (0.99) and pyrite (0.99) at pH 7 are larger compared to those for Freundlich isotherm model for δ-$MnO_2$ (0.94) and pyrite (0.94). Similar trends were found for pH of 8 (Table 2), suggesting that the sorption of $V^V$ on the mineral surface likely occurs with respect to homogeneous sites (Seader et al., 1998).

Fitting sorption data to the Langmuir isotherm model leads to the estimates of the maximum adsorption capacity, site density, adsorption constant, and site concentration (Supplementary Data Fig. S4; Table 3). The amount of sorption of $V^V$ on δ-$MnO_2$ surface was significantly higher than that on pyrite surface for all cases (Table 3). The estimated maximum $V^V$ sorption capacity (~76.41 μmol $g^{-1}$) with respect to δ-$MnO_2$ at pH 7 is ~300 times that (~0.24 μmol $g^{-1}$) on pyrite surfaces (Table 3). The estimated site density (~0.95 sites $nm^{-2}$) for $V^V$ sorption on δ-$MnO_2$ is ~3 times that (~0.33 sites $nm^{-2}$) for $V^V$ sorption on pyrite surfaces (Table 3).

### 4.7. Impacts of ionic strength and phosphate on sorption

The sorption of $V^V$ on δ-$MnO_2$ or pyrite decreased with decreasing ionic strength. Specifically, sorption of $V^V$ on δ-$MnO_2$ decreased by ~43–54% with a decrease in NaCl concentrations from 0.7 M to 0.001 M (Fig. 6). In comparison, sorption of $V^V$ on pyrite decreased by ~24–33% with a decrease in NaCl concentrations from 0.7 M to 0.001 M (Fig. 6).

Under high ionic strength conditions (i.e., NaCl 0.7 M), the sorption of $V^V$ on δ-$MnO_2$ decreased by ~18% as phosphate concentrations increased from 0 to 20 μM. When the phosphate concentrations increased from 20 μM to 150 μM, the sorption of $V^V$ on δ-$MnO_2$ only dropped by ~4% (Fig. 6). Under low ionic strength conditions (i.e., NaCl 0.001 M), the sorption of $V^V$ on δ-$MnO_2$ decreased by ~24% as phosphate concentrations increased from 0 to 20 μM and ~2% as phosphate concentrations increased from 20 μM to 150 μM (Fig. 6).

For the case of $V^V$ sorption on pyrite at a high ionic strength (i.e., NaCl 0.7 M), the sorption of $V^V$ on pyrite decreased by ~10% as phosphate concentrations increased from 0 to 20 μM and ~2% as phosphate

**Table 2**
Freundlich and Langmuir isotherm parameters for V sorption on δ-$MnO_2$ and pyrite obtained by nonlinear fitting for different pH values.

| | Model | Parameters | pH = 7 | | pH = 8 | |
|---|---|---|---|---|---|---|
| | | | Value | S.E.[e] | Value | S.E. |
| δ-$MnO_2$ | Freundlich | $K_F$ ($\mu mol^{1-n}$ $g^{-1}$ $L^n$)[a] | 31.594 | 4.342 | 17.526 | 2.034 |
| | | $n$ | 5.003 | 0.784 | 4.192 | 0.460 |
| | | $r^2$ | 0.940 | — | 0.964 | — |
| | | SSE | 8.960 | — | 4.133 | — |
| | Langmuir | $q_m$(μmol $g^{-1}$)[b] | 76.412 | 1.881 | 52.994 | 2.454 |
| | | $K_L$(L $\mu mol^{-1}$)[c] | 1.834 | 0.272 | 0.357 | 0.061 |
| | | $r^2$ | 0.990 | — | 0.971 | — |
| | | SSE[d] | 3.640 | — | 3.812 | — |
| pyrite | Freundlich | $K_F$ ($\mu mol^{1-n}$ $g^{-1}$ $L^n$) | 0.087 | 0.011 | 0.036 | 0.004 |
| | | $n$ | 4.693 | 0.663 | 4.081 | 0.733 |
| | | $r^2$ | 0.944 | — | 0.962 | — |
| | | SSE | 0.023 | — | 0.087 | — |
| | Langmuir | $q_m$(μmol $g^{-1}$) | 0.2434 | 0.005 | 0.121 | 0.004 |
| | | $K_L$(L $\mu mol^{-1}$) | 0.2893 | 0.037 | 0.156 | 0.031 |
| | | $r^2$ | 0.991 | — | 0.983 | — |
| | | SSE | 0.009 | — | 0.007 | — |

[a] $K_F$ ($\mu mol^{1-n}$ $g^{-1}$ $L^n$) is the distribution coefficient.
[b] $q_m$ (μmol $g^{-1}$) is the maximum adsorption capacity.
[c] $K_L$ (L $\mu mol^{-1}$) is the adsorption constant related to the binding energy.
[d] *SSE* is standard error of the estimate.
[e] *S.E.* is standard error which is equal to one standard deviation (1σ).

**Table 3**
Langmuir adsorption parameters for V sorption on δ-$MnO_2$ and pyrite.

| | pH | $K_L$[a] (L $\mu mol^{-1}$) | $q_m$[b] (μmol $g^{-1}$) | $q_m$[c] (μmol $m^{-2}$) | Site density (sites $nm^{-2}$) | Site concentration[d] (μmol $L^{-1}$) |
|---|---|---|---|---|---|---|
| δ-$MnO_2$ | 7 | 1.83 | 76.41 | 1.58 | 0.95 | 38.21 |
| | 8 | 0.36 | 52.99 | 1.09 | 0.66 | 26.49 |
| Pyrite | 7 | 0.29 | 0.24 | 0.55 | 0.33 | 0.12 |
| | 8 | 0.16 | 0.12 | 0.27 | 0.16 | 0.06 |

[a] $K_L$ (L $\mu mol^{-1}$) is the adsorption constant related to the binding energy.
[b] $q_m$ (μmol $g^{-1}$) is the maximum adsorption capacity.
[c] Calculated using measured BET surface areas for δ-$MnO_2$ (48.32 $m^2$ $g^{-1}$) and pyrite (0.44 $m^2$ $g^{-1}$).
[d] Calculated from surface coverage.

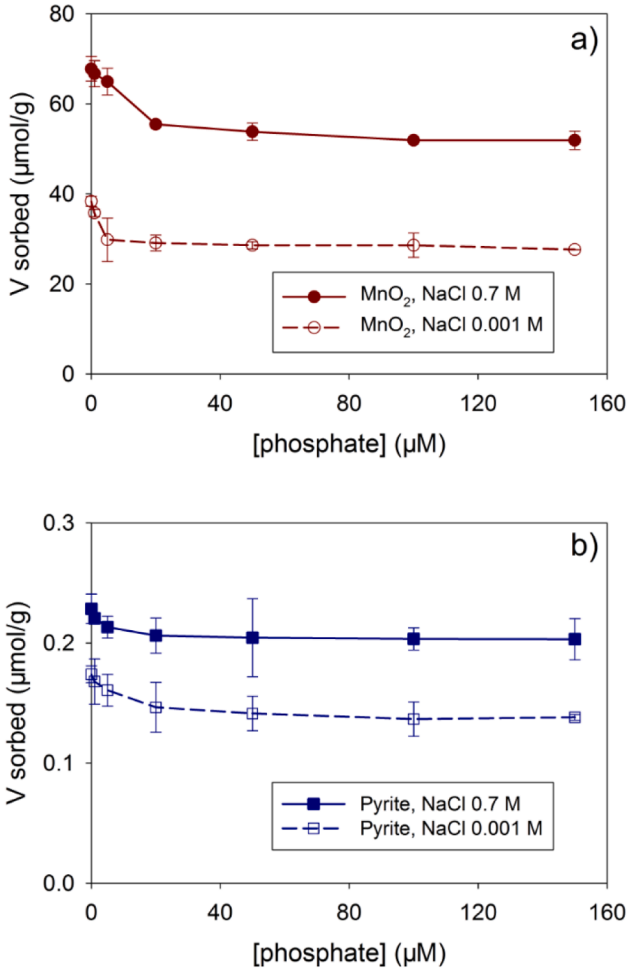


**Fig. 6.** Sorption of V onto (a) δ-$MnO_2$ and (b) pyrite as a function of phosphate concentrations at pH 7 for ionic strength 0.7 M and 0.001 M, respectively. Error bars are equal to one standard deviation (1σ) based on two replicates.

concentrations increased from 20 μM to 150 μM. In the low ionic strength experiments (i.e., NaCl 0.001 M), the sorption of $V^V$ on pyrite decreased by ~16% as phosphate concentrations increased from 0 to 20 μM. As phosphate concentrations increased from 20 μM to 150 μM, the sorption of $V^V$ on pyrite dropped by ~5% (Fig. 6).

## 5. Discussion

### 5.1. Concentration pattern of dissolved vanadium in the Chesapeake Bay

The concentration patterns of vanadium in the Chesapeake Bay differ between oxic, suboxic zone (i.e., where there is no detectable oxygen or sulfide), and sulfidic waters indicating that different geochemical and redox processes influence vanadium distributions in these settings. Dissolved vanadium concentrations remain stable at values of 15.0–17.2 nM in the top part of the water column where $O_2$ concentrations are >84 μM. There are no data points in the measured $O_2$ concentrations between 35 and 84 μM. For $O_2$ concentration data between non-detectable and 35 μM in deeper portions of the water column, dissolved vanadium concentrations show a positive correlation with $O_2$ concentrations ($R = 0.97$, $p < 0.01$, n = 6; Fig. 7). Extending this line to the stable vanadium concentrations of 15–17.2 nM gives a $O_2$ concentration value of 50–60 μM, which is normally defined as hypoxic water (Roman et al., 2019). Dissolved vanadium concentrations generally show a negative correlation with dissolved Mn concentrations in the oxic and hypoxic portions of the water column ($R = –0.78$, $p < 0.01$, $n = 11$; Fig. 7). Dissolved vanadium concentrations increase with depth in anoxic waters containing dissolved sulfide in both the water column and sediment porewaters (Fig. 2). Previous studies by Oldham et al. (2017) showed that Mn oxides accumulated and formed a peak above the sulfidic zone, but below the oxic zone, in a location in the Chesapeake Bay close to our Site-858, similar to other redox stratified euxinic systems such as the Baltic Sea and the Black Sea (Konovalov et al., 2003; Trouwborst et al., 2006; Bauer et al., 2017; Dellwig et al., 2019). Simultaneous Mn(IV) reduction and Mn(II) oxidation can occur in this hypoxic zone through different reduction mechanisms such as microbial reduction, chemical reduction or Mn–binding ligand formation (Tebo et al., 1991; Dollhopf et al., 2000; Oldham et al., 2017). Therefore, the relationship between $O_2$ and V hints at coupled Mn reduction and oxidation, and the positive correlation between dissolved vanadium and dissolved $O_2$ is actively linked to the formation of Mn oxides in the hypoxic zone.

On the other hand, in sulfidic portions of the water column and sediment pore waters, we found a positive relationship between dissolved vanadium and dissolved Mn ($R = 0.98$, $p < 0.01$, $n = 24$; Fig. 7c). This suggests that the increasing vanadium below the chemocline is likely sourced via desorption from Mn oxides and/or Mn oxide dissolution processes (Balistrieri and Murray, 1986; Morford et al., 2005; Beck et al., 2008; Chappaz et al., 2008). Dissolved vanadium concentrations and $H_2S$ concentrations are also positively correlated in the sulfidic zone of the water column and sediment pore waters ($R = 0.96$, $p < 0.01$, $n = 21$; Fig. 7d). In sulfidic waters, the formation of pyrite may

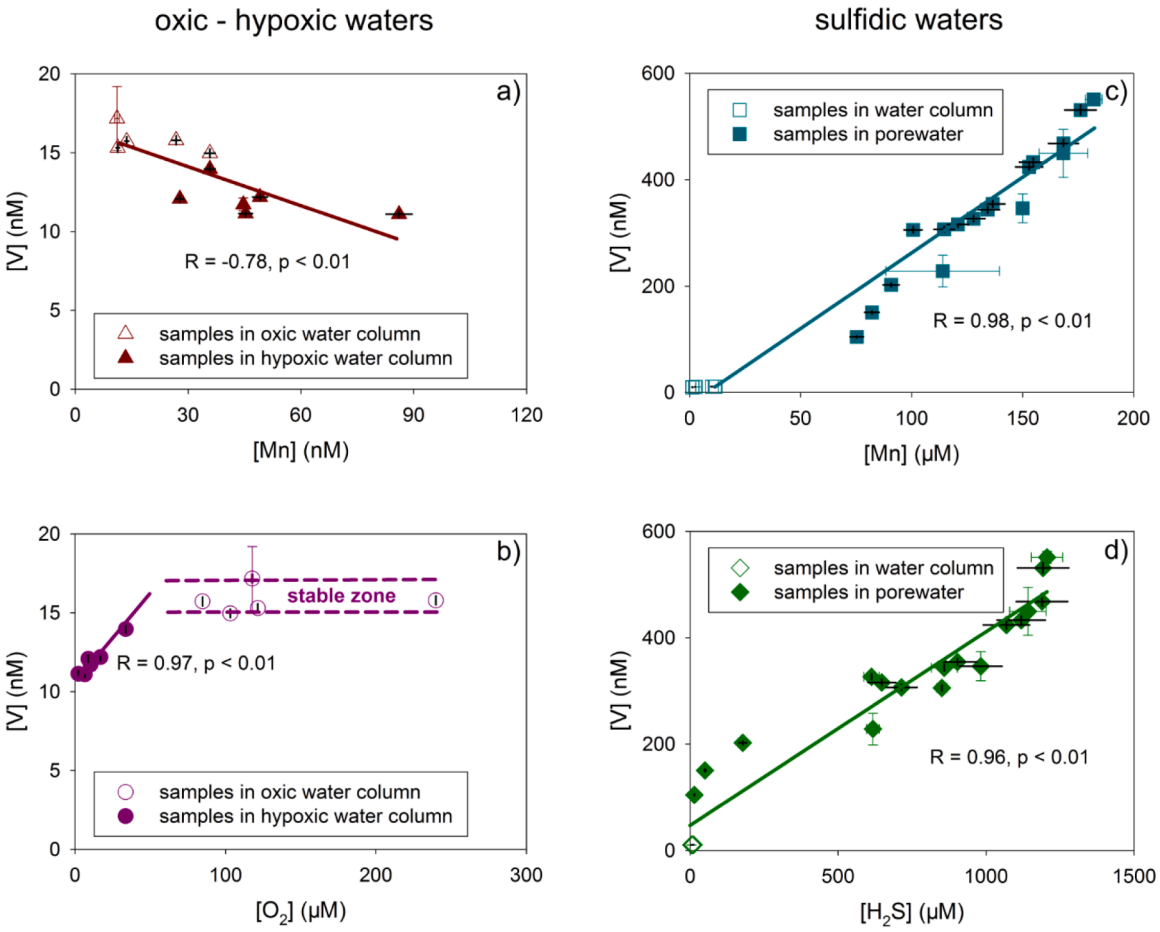


**Fig. 7.** Dissolved V concentrations as a function of dissolved Mn concentrations (a) and $O_2$ concentrations (b) in oxic – hypoxic water column to ~19 m (i.e., not sulfidic). Dissolved V concentrations as a function of dissolved Mn concentrations (c) and $H_2S$ concentrations (d) in sulfidic waters. Oxic zone has $O_2$ concentrations > 84 μM, where hypoxic zone has $O_2$ concentrations < 60 μM. Error bars with any color other than black are equal to one standard deviation (1σ) with two replicates. Error bars with black color represent the standard error for a single measurement.

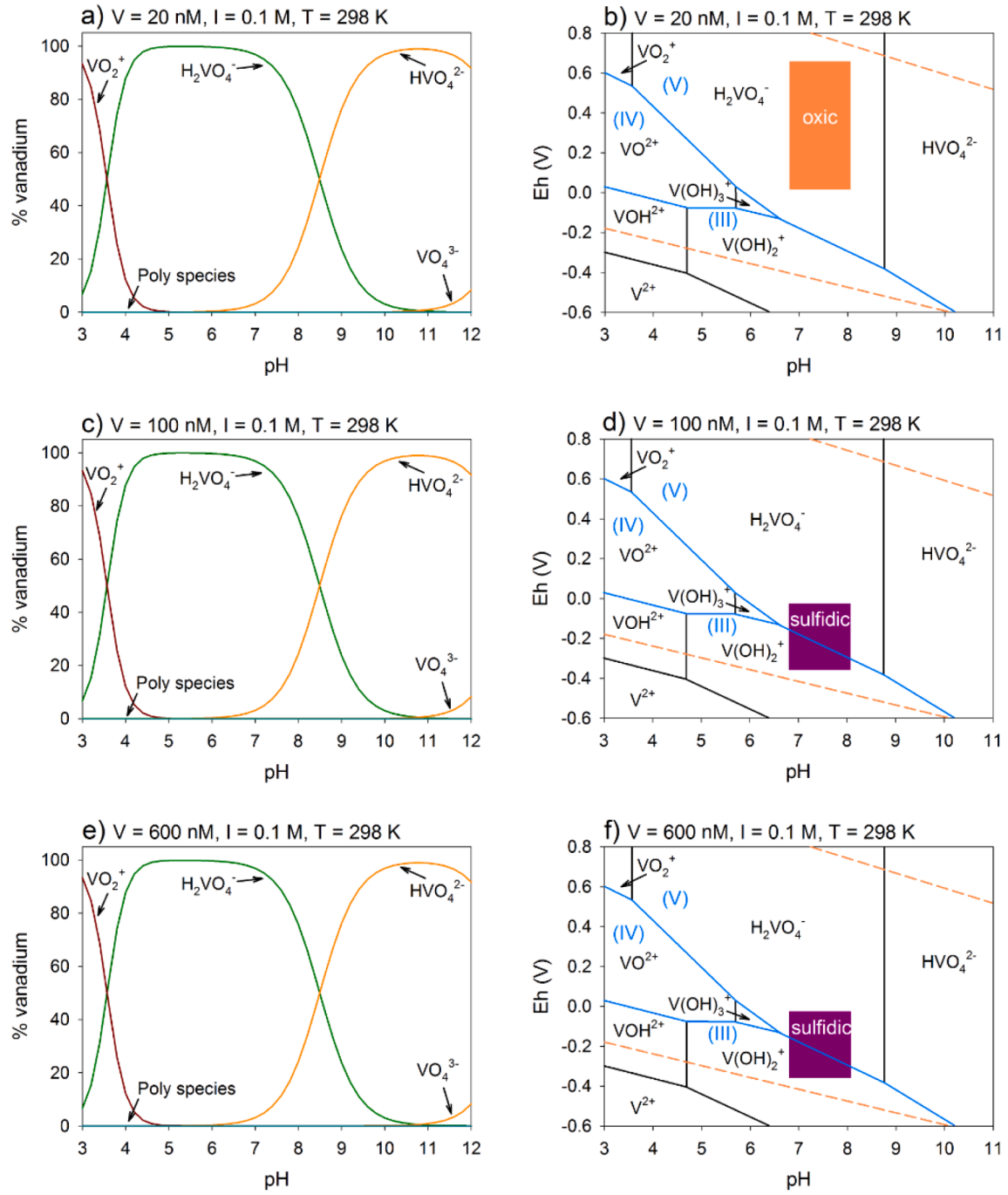


**Fig. 8.** Modeled speciation of monomeric and polymeric vanadate as a function of pH and modeled predominance diagram showing the vanadium speciation as a function of pH and Eh using (a, b) [V] = 20 nM, Ionic Strength (I) = 0.1 M (as NaCl), (c, d) [V] = 100 nM, I = 0.1 M, and (e, f) [V] = 600 nM, I = 0.1 M, at T = 298 K. The blue solid lines separate the predominance fields of the three oxidation states (III), (IV), and (V) for V. The orange dashed lines in panels (b), (d), (f) indicate the limit of stability of water with respect to $H_2(g)$ (at low Eh values) and $O_2(g)$ (at high Eh values). Orange area in panel (b) indicates V speciation in oxic water column for the study site 858 of the Chesapeake Bay. Purple areas in panels (d) and (f) indicate V speciation in sulfidic waters for the study site 858 of the Chesapeake Bay. The speciation of monomeric and polymeric vanadate only involves the $V^V$ species in solution and the corresponding stability constants employed are provided in Table S1. The Eh-pH predominance modeling involves $V^{III}$, $V^{IV}$, and $V^V$; the stability constants for $V^{III}$ and $V^{IV}$ species are from MINTEQ version 2.4 database, and the stability constants for $V^V$ species are provided in Table S1.

limit dissolved vanadium concentrations via sorption processes. In addition, $V^V$ (i.e., $H_2V^VO_4^{2-}$; Fig. 8) in the water column may convert to $V^{III}$ species in pore waters, which is thermodynamically stable in sulfidic waters (i.e., $V^{III}(OH)_2^+$; Fig. 8). Because $V^{III}(OH)_2^+$ hydrolyzes in aqueous solution, this may subsequently lower the dissolved vanadium concentrations due to the precipitation of $V^{III}(OH)_3(s)$ (Wanty and Goldhaber, 1992). In both these cases (i.e., vanadium sorption on pyrite and $V^{III}(OH)_3$ precipitation), we would expect dissolved vanadium and $H_2S$ concentrations to be negatively correlated. In contrast, we find a positive relationship ($R = 0.96$, $p < 0.01$, $n = 21$; Fig. 7d), suggesting that the influence of both processes may be limited. To further investigate what are the key processes that influence the vanadium geochemistry in sulfidic waters, we conducted experiments to investigate the sink of vanadium by adsorption on Mn oxides, pyrite, and the precipitation of

$V^{III}(OH)_3$ during vanadium reduction by $H_2S$. Manganese oxides are investigated because their formation and stability in overlying oxic and suboxic waters and reductive dissolution in sulfidic waters (e.g., Oldham et al., 2017) can affect vanadium cycling.

### 5.2. Vanadium(V) sink by adsorption to Mn oxides and pyrite, and reduction by $H_2S$

The experiment results suggest that vanadium adsorption was greater and more rapid on δ-$MnO_2$ compared to pyrite (Table 1). Initial sorption of vanadium on both δ-$MnO_2$ and pyrite occurred within 30 min (Fig. 4). In contrast, there was no response in vanadium sink within 90 min (referred to as induction period) in the presence of $H_2S$ (Fig. 4). Wanty and Goldhaber (1992) studied the reduction of $V^{IV}$ to $V^{III}$ by measuring $V^{III}$ in precipitates that formed in the presence of various $H_2S$ concentrations (>5.5 mM). The observed induction times (~1.5–3 h) in our study are in good agreement with those observed in Wanty and Goldhaber (1992). However, these researchers found that under low pH values (i.e., pH < ~6), the induction periods were much longer (~10–310 h; Wanty and Goldhaber, 1992). In addition, Wanty and Goldhaber (1992) found that an increase in $H_2S$ concentrations (from ~5.5 mM to ~27.5 mM) led to an increase in the induction period (from ~102 h to ~150 h) and decrease in reduction rates. These researchers attribute this observation to ionic strength differences but eventually found ionic strength may not appreciably impact the vanadium reduction processes (Wanty and Goldhaber, 1992). In contrast, we found that the induction periods for vanadium sink appear to be shorter with increasing $H_2S$ concentrations (Fig. 4). Under our experimental pH condition (i.e., pH ~7), the thermodynamically stable vanadium species in anoxic waters are $H_2V^VO_4^-$ and $V^{III}(OH)_2^+$, respectively (Fig. 8). In contrast, under low pH values (i.e., pH < 6; Wanty and Goldhaber, 1992), the thermodynamically stable vanadium species can be $H_2V^VO_4^-$, $V^{III}(OH)_2^+$, $V^{IV}O^{2+}$, $V^{IV}(OH)_3^+$, or $V^{III}OH^{2+}$ once reducing conditions are met (Fig. 8). It should be noted that $V^{II}$ is not likely to form because it is outside the stability limit of water and that there is a narrow range for $V^{IV}(OH)_3^+$ stability that does not overlap our field conditions (Fig. 8b, d, f). Hence, the geochemical behavior of vanadium may differ greatly with respect to different vanadium species, implying vanadium geochemistry is very sensitive to pH conditions in anoxic waters.

The sink of vanadium from aqueous solution by both sorption on pyrite and reduction by sulfide is lower than that by sorption on δ-$MnO_2$. For example, at equilibrium dissolved vanadium decreased by ~74–97% in solutions with δ-$MnO_2$ at pH 8, whereas dissolved vanadium decreased by ~15–39% and ~1–3% in solutions with pyrite and $H_2S$, respectively (Fig. 4). This suggests that increased vanadium concentrations in sulfidic waters (Figs. 2, 7) may be attributed to the substantial release of vanadium due to desorption from and/or dissolution of Mn oxides in the presence of $H_2S$, overcoming the sink by sorption on pyrite and/or by $H_2S$ reduction to $V(OH)_3$. Sorption to other iron sulfide minerals such as greigite or mackinawite (Vessey and Lindsay, 2020) may also affect V patterns if these minerals form in the water column and subsequently dissolve in the porewaters, releasing sorbed metals to the porewater (Rickard, 2012). However, given that dissolved vanadium is highly correlated with dissolved Mn and $H_2S$ in the sulfidic zone (Fig. 7), it is likely that much of the V patterns in the water column are determined by reductive dissolution of Mn oxides. It should be noted that vanadium reduction in the presence of $H_2S$ did not reach equilibrium over the course of the experiment (~3600 mins; Fig. 4). Nonetheless, while dissolved vanadium concentrations may decrease as waters become more reducing due to sink by sorption on pyrite, other iron sulfide minerals, and/or by $V(OH)_3$ formation by $H_2S$ reduction, our observational and experimental results indicate Mn cycling plays a more important role in determining dissolved vanadium concentration patterns.

Sorption of vanadium occurs at pH > 4, which is higher than the point of zero charge (PZC) value of δ-$MnO_2$ (~3.0; McKenzie, 1981) or PZC value of pyrite (~2.4; Widler and Seward, 2002). This indicates that electrostatic attraction is not the only factor controlling vanadium sorption, as has been shown for other minerals or soils (Blackmore et al., 1996; Brinza et al., 2008; Larsson et al., 2017a; Zhu et al., 2018). The plots of vanadium adsorption on δ-$MnO_2$ and pyrite for the intraparticle diffusion model show rapid initial adsorption (i.e., within ~2–5 min) for vanadium sorption on both δ-$MnO_2$ and pyrite (Supplementary Data Fig. S3c, f), which reflects adsorption on external surfaces. After rapid initial external sorption, we find that the timescale for the subsequent vanadium sorption into pore spaces (intraparticle diffusion) lasts about 2–4 h for δ-$MnO_2$ and 20 h for pyrite, respectively (Supplementary Data Fig. S3). As such, the intraparticle diffusion step was likely the rate controlling step for vanadium sorption. However, because the plots of vanadium sorption for the intraparticle diffusion model do not pass through the origin point ($C \neq 0$), this implies that intraparticle diffusion step is not the only rate-controlling step (Ranjan et al., 2009).

The observation that the experimental data aligns with the pseudo-second-order model (Table 1) suggests that the chemical sorption is the rate-controlling mechanism (Ho and McKay, 1999; Wu et al., 2001). Therefore, higher rates ($h$) for vanadium sorption on δ-$MnO_2$ than those for vanadium sorption on pyrite imply that there is a stronger chemical bonding between vanadium and δ-$MnO_2$ compared to that between vanadium and pyrite (Table 1). This is consistent with the notion that $V^V$ prefers O atoms over S atoms because lower oxidation states prefer S atoms, higher oxidation states prefer O atoms, which is based on the hard-soft acid base theory (Pearson, 1988; Luther III, 2016).

The Langmuir isotherm also provides a good fit to the vanadium sorption data (Table 2), indicating that vanadium species primarily sorb to a specific number of active sites in a single layer. The monolayer capacities correspond to the site densities for vanadium of ~1 sites $nm^{-2}$ and ~0.7 sites $nm^{-2}$ on δ-$MnO_2$, at pH 7 and 8, respectively (Table 3). The estimated site densities correspond to ~0.25 reactive sites/unit cell for pH 7 or ~0.18 reactive sites/unit cell for pH 8, assuming the sites are uniform and sorb tetrahedral $H_2V^VO_4^-$ (Supplementary Data Fig. S2). This suggests that not all surface functional groups are reactive. In comparison, monolayer capacities correspond to site densities for vanadium of ~0.3 sites $nm^{-2}$ and ~0.2 sites $nm^{-2}$ on pyrite, at pH 7 and 8, respectively (Table 3) with corresponding reactive sites/unit cell of ~0.08 for pH 7 and ~0.05 for pH 8, respectively. We estimated the Gibbs free energy for sorption of vanadium using the equation below (Parfitt and Rochester, 1983):

$$\Delta G^0 = -RT\ln K_L \quad (7)$$

in which, R is the gas constant with a value of 8.314 J $K^{-1}$ $mol^{-1}$, T is temperature (Kelvin), and $K_L$ (L $mol^{-1}$) is sorption constant from eq. (6). The estimated Gibbs free energy of vanadium surface sorption is more negative for δ-$MnO_2$ (–35.34 ± 0.51 kJ $mol^{-1}$ at pH = 7 and –31.32 ± 0.60 kJ $mol^{-1}$ at pH = 8) than for pyrite (–30.82 ± 0.44 kJ $mol^{-1}$at pH = 7 and –29.27 ± 0.71 kJ $mol^{-1}$ at pH = 8). These results suggest that vanadium sorption occurs more favorably on δ-$MnO_2$ than pyrite.

The observation that only a fraction of vanadium adsorbed on δ-$MnO_2$ and pyrite was released during the desorption titration when pH increased from ~6 to ~8 implies that a large fraction of the vanadium was strongly bonded on the surface, possibly via inner-sphere complexes (Fig. 5). The fraction of vanadium that remains sorbed to δ-$MnO_2$ at pH ~7–8 (~48–72%) is higher than that for pyrite (~15–29%; Fig. 5), implying that (1) the strength of inner-sphere complexes of vanadium on δ-$MnO_2$ surfaces is greater than those on pyrite surfaces; (2) the process is much controlled by the hard-soft acid base theory such that $V^V$ prefers O atoms over S atoms (Pearson, 1988; Luther III, 2016).

The amount of vanadium sorbed to mineral surfaces decreases with increasing phosphate concentrations (Fig. 6), which indicates that sorption of vanadium on mineral surface is influenced to a limited extent by phosphate as we now show. Wehrli and Stumm (1989) studied the sorption of vanadium onto $TiO_2$ and δ-$Al_2O_3$ surfaces and found that

different inner-sphere complexes may form under different pH conditions. These researchers further proposed the formation of inner-sphere, monodentate $SOVO_3H^-$ surface complexes via exchange of a single surface hydroxyl $OH^-$ for $HVO_4^{2-}$ (Wehrli and Stumm, 1989). Peacock and Sherman (2004) found that the sorption of vanadate on goethite is strong and involves the formation of inner-sphere complexes $VO_2(OH)_2$ and $VO_3(OH)$. These researchers attributed the formation of inner-sphere surface complexes to the bidentate corner-sharing processes with surface complexes formed (i.e., $Fe_2O_2V(OH)_2^+$ and $Fe_2O_2VO(OH)^0$; Peacock and Sherman, 2004). Larsson et al. (2017b) studied the sorption of vanadate and vanadyl (i.e., $V^{IV}$) on ferrihydrite and found both vanadate and vanadyl were adsorbed as tetrahedral vanadate (i.e., $V^VO_4^{3-}$), with the formation of inner-sphere edge-sharing bidentate complexes. Brinza et al. (2019) studied vanadium and molybdenum sorption on ferrihydrite and found differences in inner-sphere complexes formed between vanadium and molybdenum. While we lack constraints on the chemistry of the surface complexes formed on δ-$MnO_2$ or pyrite, the experimental results imply that strong inner-sphere complexes formed may limit the sorption inhibition by phosphate. One possible explanation is that the sorption of phosphate dianion occupied the sites for vanadate. As such, phosphate partially decreases vanadate adsorption and does not outcompete vanadate as we observed in Fig. 6. To extend this to a natural system, concentrations of phosphate range from ~0 to ~3 μM at a nearby study site (CB3.3C) in the Chesapeake Bay (Li et al., 2017). The corresponding inhibitions are estimated to be ~4–15% for δ-$MnO_2$ and ~6–8% for pyrite, respectively (Fig. 6). This implies that the impact of phosphate on vanadium sorption is likely to be limited in natural waters with similar phosphate concentrations to <15%.

Sorption of vanadium on δ-$MnO_2$ or pyrite decreased with decreasing ionic strength (Fig. 6). Similar decreases in sorption were observed for vanadate, phosphate, borate, or arsenate adsorption on different minerals (Goldberg et al., 1993; Arai and Sparks, 2001; Cornu et al., 2003; Li et al., 2013; Wainipee et al., 2013; Zhu et al., 2018). The increase of $Na^+$ concentrations may facilitate $Na^+$–anion co-adsorption, in which $Na^+$ was adsorbed and possibly acted as a positively charged bridge that can facilitate vanadium sorption via electrostatic attraction (Arai and Sparks, 2001; Li et al., 2013; Wainipee et al., 2013; Zhu et al., 2018). In addition, both mineral surfaces are towards more negative when ionic strength becomes lower. This leads to an enhanced repelling force for $V^V$ and causes a lower sorption of V. Alternatively, the higher sorption at high ionic strength may be attributed to a transition from outer-sphere complexes to inner-sphere complexes, as suggested by McBride (1997), which subsequently enhances the sorption of vanadium on δ-$MnO_2$ or pyrite surfaces. Ionic strength generally ranges from low values (0–0.005 M; Domenico and Schwartz, 1998) in freshwater through estuarine waters to high values in seawater (~0.7 M). Hence, the sorption of vanadium on mineral surfaces may be lower in freshwater environments compared to marine environments.

### 5.3. Relationship between Mn and V burial in sulfidic waters

Experimental results support the conclusion that the positive correlation between dissolved vanadium and dissolved $O_2$ in oxic waters is likely due to the sorption of vanadium on Mn oxides, whereas the positive correlation between dissolved vanadium and Mn in sulfidic waters is likely due to desorption and/or dissolution processes (Figs. 5–7). While solid phase V/Ti and Mn/Ti ratios both increase with depth (Fig. 3d, e) and show a positive correlation ($R = 0.79$, $p < 0.01$, $n = 15$; Fig. 9a), the ratios of V/Mn decrease with depth and are negatively correlated with $H_2S$ concentrations in sulfidic waters ($R = -0.8$, $p < 0.01$, $n = 15$; Fig. 9c). This decrease in solid phase V/Mn with depth is countered by an increase in dissolved V/Mn molar ratios, which show a positive linear relationship with $H_2S$ concentrations in sulfidic waters ($R = 0.84$, $p < 0.01$, $n = 17$; Fig. 9b). These results suggest that manganese cycling plays a key role in determining vanadium geochemistry; therefore, sedimentary V/Mn ratios are a useful tool in addition to existing paleoredox proxies.

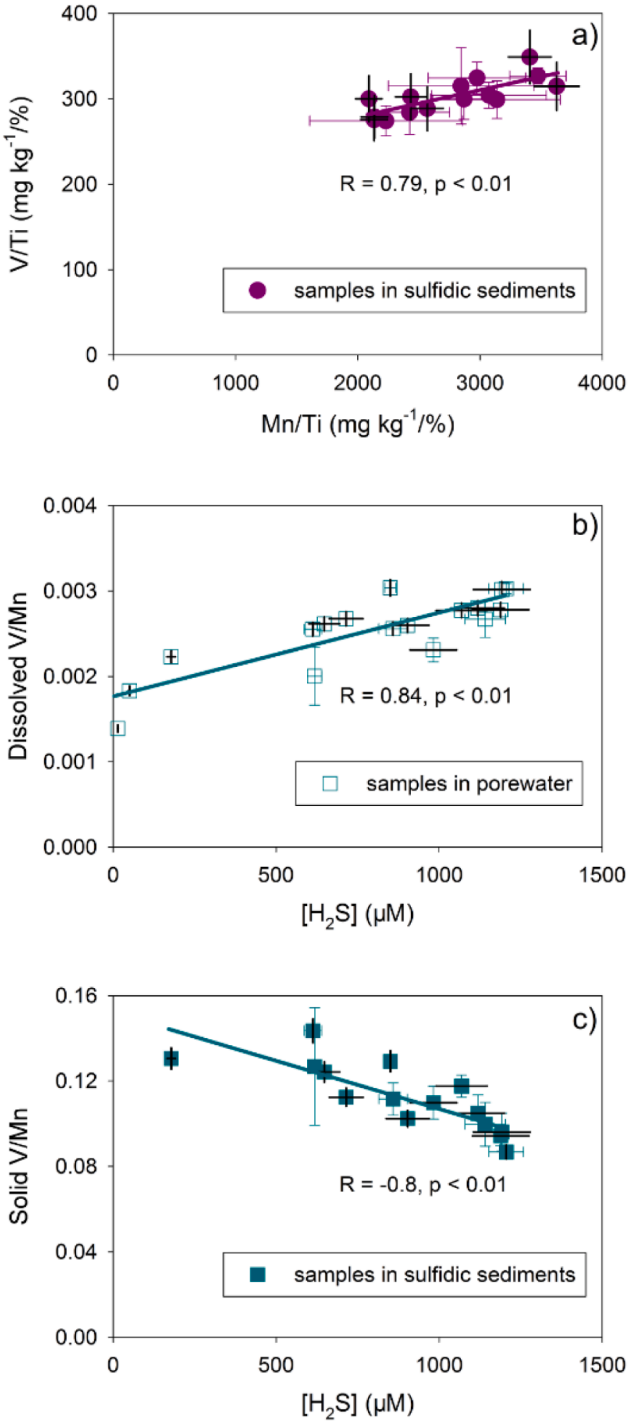


**Fig. 9.** Dependence of (a) solid phase V/Ti ratios on solid phase Mn/Ti ratios in sulfidic sediments, (b) dissolved V/Mn ratios on $H_2S$ concentrations in sulfidic waters, and (c) solid phase V/Mn molar ratios on $H_2S$ concentrations in sulfidic waters. Error bars with any color other than black are equal to one standard deviation (1σ) based on two replicates. Error bars with black color represent the standard error for a single measurement. V/Mn molar ratio (i.e., μM/μM) is unitless.

As discussed above, the positive relationship between dissolved vanadium and $H_2S$ is attributed to the substantial release of vanadium due to desorption from and/or dissolution of Mn oxides in the presence of $H_2S$, which has a controlling influence on vanadium geochemistry than

sorption on pyrite and/or reduction by $H_2S$ to form solid $V(OH)_3$. Importantly, the increase in solid phase Mn with depth is not likely due to the formation of Mn oxides, but rather the incorporation of Mn into authigenic pyrite (Olson et al., 2017). Thus, the V/Mn molar ratio also reflects the impact of sulfide and other major redox-sensitive geochemical processes that impact the dissolved and solid phase vanadium concentrations. As a consequence, the V/Mn molar ratios are recommended over vanadium concentrations for investigating redox changes in aquatic environments. Specifically, solid phase V/Mn molar ratios decrease as waters become more sulfidic (Fig. 9).

It should be noted that despite the general trend that dissolved V/Mn molar ratios decrease along with oxygen levels in oxic water column (Fig. 2c), this is not necessarily accompanied by an increase in solid phase V/Mn molar ratios. For example, data from the Landsort Deep of the Baltic Sea shows that both dissolved and solid phase V/Mn molar ratios decrease as dissolved oxygen decrease in the oxic water column (Bauer et al., 2017). Additionally, data from oxic surface sediments suggests that solid phase V/Mn molar ratios are lower and less variable than those in anoxic, non-sulfidic sediments (Bennett and Canfield, 2020).

Specifically, the median value (92.0 μg $g^{-1}$/%) of V enrichments (note: the V enrichments V/Al is used here, where V enrichment = Vanadium concentration (μg $g^{-1}$)/Aluminum concentration (%)) in the perennial oxygen-minimum zone (OMZ) is ~3 times that (29.5 μg $g^{-1}$/%) of restricted euxinic basins as shown in previous studies (Piper and Dean, 2002; Böning et al., 2004; Lüschen, 2004; Borchers et al., 2005; Scholz et al., 2011; Bennett and Canfield, 2020). This is also true that V enrichments are much higher in perennial OMZ, compared with V enrichments in this study of a site with seasonal water column sulfide accumulation of 15.7 μg $g^{-1}$/%. One possible explanation is that large flux of particulate organic matter and Fe/Mn-(oxyhydr)oxides can adsorb dissolved V and carry it to the seafloor in OMZ environments (Scholz et al., 2011, 2018; Bennett and Canfield, 2020). This is also consistent with our experimental results that V adsorption is greater on δ-$MnO_2$ compared to pyrite. The median V/Mn molar ratios (~2.3) in perennial OMZ are ~3 times that of V/Mn molar ratios (~0.7) in restricted euxinic basins (Piper and Dean, 2002; Böning et al., 2004; Lüschen, 2004; Borchers et al., 2005; Scholz et al., 2011; Bennett and Canfield, 2020). This suggests the possibility of using a high V enrichment coupled with a high V/Mn ratio to indicate deposition below an oxygen-minimum zone.

### 5.4. *Application of V/Mn ratios for ancient ocean redox changes*

We now consider how V/Mn data from black shales that span the Proterozoic, and Phanerozoic compiled in the Sedimentary Geochemistry and Paleoenvironments Project record information about variations in the extent of anoxic, non-sulfidic marine waters (Farrell et al., 2021). To evaluate changes in V/Mn with time, we plotted the interquartile range and median, as well as employing the rolling mean approach used in Large et al. (2014). For the sake of completeness, we plot V/Mn going back to the Archean, but do not make interpretations about this time period due to uncertainties in the biogeochemical processes that impacted sedimentary Mn concentrations from ~2500 Ma to ~2000 Ma and their links with the Great Oxidation Event (*cf.* Johnson et al., 2013; Jones and Crowe, 2013).

There are large variations in V/Mn molar ratios superimposed upon an increasing trend from ~600 Ma to ~540 Ma (Fig. 10d). These patterns occur in association with the Neoproterozoic oxygenation event (NOE), which has been argued to occur as early as 800 Ma (see review in Lyons et al., 2021) or after the Marinoan Glaciation (~630 Ma; Yuan et al., 2011; Sahoo et al., 2012) and prior to the late Ediacaran (~580–550 Ma; Fike et al., 2006; Canfield et al., 2007; Scott et al., 2008). Previous studies have estimated that ~9 × $10^{17}$ kg of $O_2$

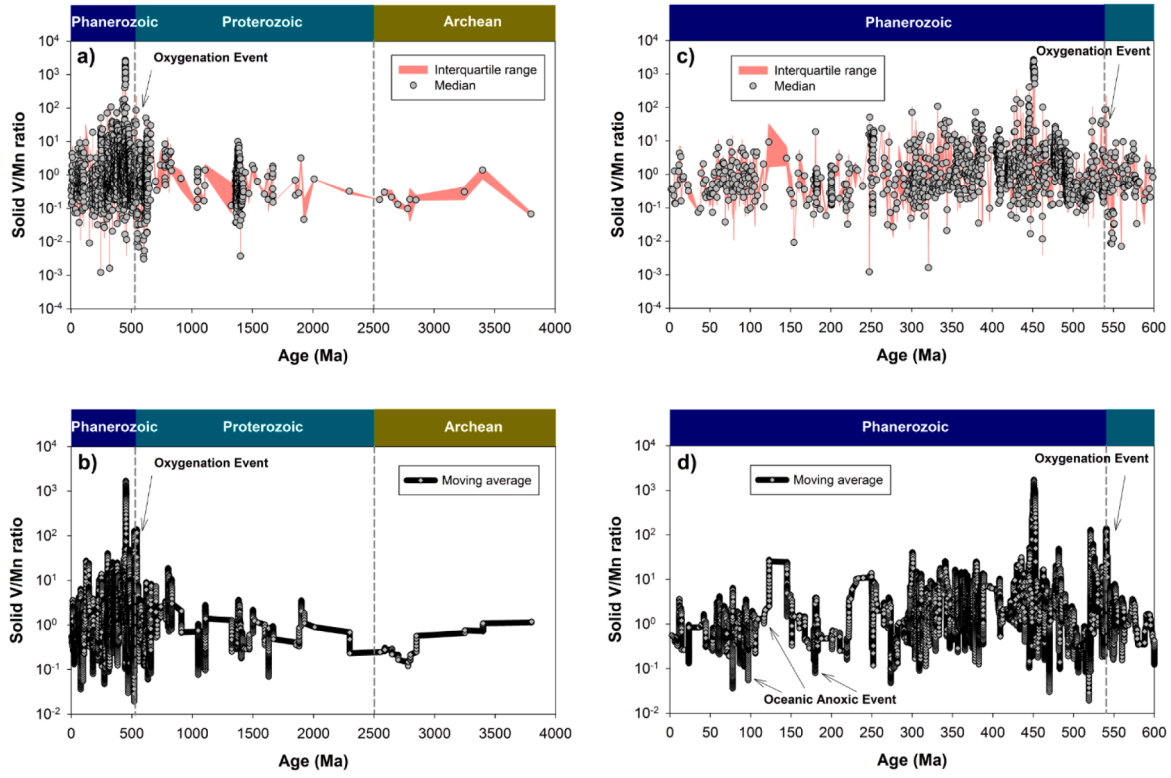


**Fig. 10.** (a) The median and interquartile range for V/Mn molar ratios in black shales from ~3800 Ma of the Archean (yellow color) via the Proterozoic (cyan color) to the Phanerozoic (blue color). (b) Moving averaged trends (19 points rolling mean) for V/Mn molar ratios in the black shales with the same time range in panel (a). The higher resolution of data series for the Phanerozoic (blue color) in panel (a, b) are given in panel (c, d). V/Mn molar ratio (i.e., μM/μM) is unitless. Data of V and Mn were from Sedimentary Geochemistry and Paleoenvironments Project available in the Supplementary Data.

accumulated in the atmosphere (Canfield, 2005; Campbell and Squire, 2010) and this increase has been proposed to be linked to the first appearance of animals (Narbonne and Gehling, 2003; Canfield et al., 2007). An important potential effect of rising atmospheric oxygen on the marine realm is an increase in sulfide oxidation (Kunzmann et al., 2017). The increase in sedimentary V/Mn record is consistent with an increase in anoxic, non-sulfidic marine conditions as a result of the NOE, which is also supported by iron speciation data (Sperling et al., 2015). As such, the trends in V/Mn molar ratios during NOE may imply that atmospheric oxygenation lead to enhanced sulfide oxidation in the time period leading up to the end of the Neoproterozoic (~540 Ma).

In addition to providing information about the impacts of the NOE, V/Mn molar ratios show decreasing trends through time as well that are linked with the expansion of sulfidic (i.e., euxinic) marine conditions. For example, decreases in V/Mn molar ratios at ~183 Ma, ~120 Ma, and ~94 Ma (Fig. 10d) support an increase in reducing conditions in the ocean during the Toarcian, Early Aptian, and Cenomanian/Turonian Oceanic Anoxic Events (T-OAE, OAE1a, and OAE2 respectively; Meyers et al., 2012; Boulila et al., 2014; Huang and Hesselbo, 2014; Sell et al., 2014). The sedimentary record of these events contains evidence for euxinic conditions (see compilations in Meyer and Kump, 2008; Monteiro et al., 2012).

Similar to previous studies of sedimentary rocks (Algeo and Maynard, 2004; Cruse and Lyons, 2004; Tribovillard et al., 2004, 2006), solid phase V concentrations generally increase with total organic carbon (TOC) concentrations (Supplementary Data Fig. S5). However, sediments with different TOC concentrations have different relationships between Mn and the V/Mn ratio. Specifically, the increase of TOC content is met with an increase in V/Mn ratios and a decrease in Mn concentrations (Supplementary Data Fig. S6). The plot of TOC contents against V/Mn ratios can be separated into three zones with low V values (<1000 ppm), middle V values (1000–3000 ppm), and high V values (>3000 ppm) (Supplementary Data Fig. S7). These results indicate that TOC is also important in controlling V cycling and V/Mn ratios. Therefore, consideration of the roles that Mn and TOC play in the sequestration of V into sediments makes the V/Mn ratio another important geochemical tool for studying redox conditions of past oceans.

## 6. Conclusions

We present dissolved vanadium concentration patterns in oxic, anoxic, and sulfidic zones of the water column and pore waters and corresponding vanadium enrichments in sulfidic sediments in the Chesapeake Bay. Vanadium concentrations show relationships with Mn concentrations in both aqueous and solid phases, indicating that increased concentrations of dissolved vanadium below the chemocline are due to desorption and/or dissolution processes from Mn oxides. Experimental results support this interpretation because they show that the influence of Mn oxides on vanadium geochemistry is much greater than the influence of sorption on pyrite and/or by $H_2S$ reduction to V $(OH)_3$. In addition, our experimental results indicate that the sorption of vanadium forms inner-sphere complexes. The estimated site densities for vanadium sorption on Mn oxides and pyrite indicate that not all surface functional groups are reactive. The estimated Gibbs free energy of vanadium sorption is more negative for Mn oxides than for pyrite, implying vanadium is more easily adsorbed on Mn oxides than pyrite surfaces. Furthermore, the sorption of vanadium is strongly sensitive to pH conditions and moderately sensitive to ionic strength, whereas vanadium sorption is less affected by phosphate concentrations. Our results show that when conditions become more sulfidic dissolved V/Mn molar ratios increase, while solid phase V/Mn molar ratios decrease. Because the negative relationship between solid phase V/Mn molar ratios and $H_2S$ concentrations as well as the positive relationship between dissolved V/Mn molar ratios and $H_2S$ concentrations hold simultaneously, we suggest that sedimentary V/Mn molar ratios can be a useful additional tool for extracting information about ancient ocean redox conditions.

## Declaration of Competing Interest

The authors declare that they have no known competing financial interests or personal relationships that could have appeared to influence the work reported in this paper.

## Acknowledgements

We would like to thank the captain and crew of the RV *Sharp*, as well as Brad Tebo and Emily Estes from the University of Deleware and Cecilia Howard, Christopher Holder, and Sarah Preheim from Johns Hopkins University for logistical and scientific support for the field work. Ship time was provided by NSF Chemical Oceanography grant OCE–1558738 to George Luther. Conversations with Jennifer Morford were helpful in developing ideas for this work. We would like to thank Erik Sperling for helpful suggestions on use of the SGP data. We would like to express many thanks to the many geologists, paleontologists, and geochemists who built the SGP database. We appreciate the help from Robert Holder and Daniel Viete for their assistance with data collection through the Hopkins LA–ICP–MS Facility, which was funded by the National Science Foundation (EAR Instrumentation & Facilities) Grant No. 1831766. We would like to thank Anthony Chappaz, and three anonymous reviewers whose comments and suggestions greatly improved this manuscript. In addition, we wish to thank Jeffrey Catalano and Natascha Riedinger for editorial handling and helpful suggestions on this manuscript.

## Appendix A. Supplementary material

**Supplementary Data 1.** Supplementary Fig. S1 presents the results of X-ray diffraction pattern of synthetic δ-$MnO_2$. Supplementary Fig. S2 presents speciation modeling results of V. Supplementary Fig. S3 presents sorption kinetic modeling results of V. Supplementary Fig. S4 presents Langmuir isotherms sorption results of V. Supplementary Fig. S5 presents relationship between solid phase V concentrations and TOC contents. Supplementary Fig. S6 presents relationship between solid phase Mn concentrations and V/Mn molar ratios. Supplementary Fig. S7 presents relationship between solid phase TOC contents and V/Mn molar ratios. Supplementary Table S1 presents stability constants used for simulation of aqueous vanadium speciation. Supplementary Table S2 presents quality control data for dissolved V and Mn in certified reference material (CRM) SLEW-3. Supplementary Table S3 presents quality control data for solid phase V and Mn in CRM OREAS. Supplementary Table S4 presents water column trace metal concentration data. Supplementary Table S5 presents pore water trace metal concentration data. Supplementary Table S6 presents solid phase trace metal concentration data. **Supplementary Data 2.** Vanadium and manganese concentration data for black shales from the compiled database of The Sedimentary Geochemistry and Paleoenvironments Project. Supplementary material to this article can be found online at https://doi.org/10.1016/j.gca.2023.08.008.

## References

Algeo, T.J., Maynard, J.B., 2004. Trace-element behavior and redox facies in core shales of Upper Pennsylvanian Kansas-type cyclothems. Chem. Geol. 206, 289–318.

Anschutz, P., Zhong, A., Sundby, B., Mucci, A., Gobeil, C., 1998. Burial efficiency of phosphorus and the geochemistry of iron in continental margin sediments. Limnol. Oceanogr. 43, 53–64.

Arai, Y., Sparks, D.L., 2001. ATR–FTIR spectroscopic investigation on phosphate adsorption mechanisms at the ferrihydrite–water interface. J. Colloid Interface Sci. 241, 317–326.

Balistrieri, L.S., Murray, J.W., 1986. The surface chemistry of sediments from the Panama Basin: The influence of Mn oxides on metal adsorption. Geochim. Cosmochim. Acta 50, 2235–2243.

Barling, J., Anbar, A.D., 2004. Molybdenum isotope fractionation during adsorption by manganese oxides. Earth Planet. Sci. Lett. 217, 315–329.
Bauer, S., Blomqvist, S., Ingri, J., 2017. Distribution of dissolved and suspended particulate molybdenum, vanadium, and tungsten in the Baltic Sea. Mar. Chem. 196, 135–147.
Bayon, G., Birot, D., Bollinger, C., Barrat, J.A., 2011. Multi-element determination of trace elements in natural water reference materials by ICP-SFMS after Tm addition and iron co-precipitation. Geostand. Geoanalytical Res. 35, 145–153.
Beck, A.J., Cochran, J.K., Sañudo-Wilhelmy, S.A., 2010. The distribution and speciation of dissolved trace metals in a shallow subterranean estuary. Mar. Chem. 121, 145–156.
Beck, M., Dellwig, O., Schnetger, B., Brumsack, H.-J., 2008. Cycling of trace metals (Mn, Fe, Mo, U, V, Cr) in deep pore waters of intertidal flat sediments. Geochim. Cosmochim. Acta 72, 2822–2840.
Bennett, W.W., Canfield, D.E., 2020. Redox-sensitive trace metals as paleoredox proxies: A review and analysis of data from modern sediments. Earth-Sci. Rev., 103175
Bennett, W.W., Lombi, E., Burton, E.D., Johnston, S.G., Kappen, P., Howard, D.L., Canfield, D.E., 2018. Synchrotron X-ray spectroscopy for investigating vanadium speciation in marine sediment: limitations and opportunities. J. Anal. At. Spectrom. 33, 1689–1699.
Bethke, C.M., 2022. Geochemical and Biogeochemical Reaction Modeling. Cambridge University Press.
Bethke, C.M., Farrell, B., Yeakel, S., 2018. GWB Reaction Modeling Guide. The Geochemist's Workbench, Release 12. Aqueous Solutions, LLC, Champaign, IL, 209 p.
Bian, L., Chappaz, A., Schovsbo, N.H., Sanei, H., 2022. A new vanadium species in black shales: Updated burial pathways and implications. Geochim. Cosmochim. Acta 338, 1–10.
Blackmore, D.P.T., Ellis, J., Riley, P.J., 1996. Treatment of a vanadium-containing effluent by adsorption/coprecipitation with iron oxyhydroxide. Water Res. 30, 2512–2516.
Böning, P., Brumsack, H.-J., Böttcher, M.E., Schnetger, B., Kriete, C., Kallmeyer, J., Borchers, S.L., 2004. Geochemistry of Peruvian near-surface sediments. Geochim. Cosmochim. Acta 68, 4429–4451.
Bonnissel-Gissinger, P., Alnot, M., Ehrhardt, J.-J., Behra, P., 1998. Surface oxidation of pyrite as a function of pH. Environ. Sci. Tech. 32, 2839–2845.
Borchers, S.L., Schnetger, B., Böning, P., Brumsack, H., 2005. Geochemical signatures of the Namibian diatom belt: Perennial upwelling and intermittent anoxia. Geochem. Geophys. Geosyst. 6.
Bostick, B.C., Fendorf, S., Helz, G.R., 2003. Differential adsorption of molybdate and tetrathiomolybdate on pyrite ($FeS_2$). Environ. Sci. Technol. 37, 285–291.
Boulila, S., Galbrun, B., Huret, E., Hinnov, L.A., Rouget, I., Gardin, S., Bartolini, A., 2014. Astronomical calibration of the Toarcian Stage: Implications for sequence stratigraphy and duration of the early Toarcian OAE. Earth Planet. Sci. Lett. 386, 98–111.
Breit, G.N., Wanty, R.B., 1991. Vanadium accumulation in carbonaceous rocks: A review of geochemical controls during deposition and diagenesis. Chem. Geol. 91, 83–97.
Brinza, L., Benning, L.G., Statham, P.J., 2008. Adsorption studies of Mo and V onto ferrihydrite. Mineral. Mag. 72, 385–388.
Brinza, L., Vu, H.P., Neamtu, M., Benning, L.G., 2019. Experimental and simulation results of the adsorption of Mo and V onto ferrihydrite. Sci. Rep. 9, 1–12.
Brumsack, H.-J., 2006. The trace metal content of recent organic carbon-rich sediments: Implications for Cretaceous black shale formation. Palaeogeogr. Palaeoclimatol. Palaeoecol. 232, 344–361.
Brunauer, S., Emmett, P.H., Teller, E., 1938. Adsorption of gases in multimolecular layers. J. Am. Chem. Soc. 60, 309–319.
Campbell, I.H., Squire, R.J., 2010. The mountains that triggered the Late Neoproterozoic increase in oxygen: The Second Great Oxidation Event. Geochim. Cosmochim. Acta 74, 4187–4206.
Canfield, D.E., 2005. The early history of atmospheric oxygen: Homage to Robert M. Garrels. Annu. Rev. Earth Planet. Sci. 33, 1–36.
Canfield, D.E., Poulton, S.W., Narbonne, G.M., 2007. Late-Neoproterozoic deep-ocean oxygenation and the rise of animal life. Science 315, 92–95.
Carpentier, W., Sandra, K., De Smet, I., Brige, A., De Smet, L., Van Beeumen, J., 2003. Microbial reduction and precipitation of vanadium by *Shewanella oneidensis*. Appl. Environ. Microbiol. 69, 3636–3639.
Chappaz, A., Gobeil, C., Tessier, A., 2008. Geochemical and anthropogenic enrichments of Mo in sediments from perennially oxic and seasonally anoxic lakes in Eastern Canada. Geochim. Cosmochim. Acta 72, 170–184.
Cline, J.D., 1969. Spectrophotometric determination of hydrogen sulfide in natural waters. Limnol. Oceanogr. 14, 454–458.
Coker, V.S., van der Laan, G., Telling, N.D., Lloyd, J.R., Byrne, J.M., Arenholz, E., Pattrick, R.A.D., 2020. Bacterial production of vanadium ferrite spinel (Fe, $V)_3O_4$ nanoparticles. Mineral. Mag. 84, 554–562.
Collier, R.W., 1984. Particulate and dissolved vanadium in the North Pacific Ocean. Nature 309, 441–444.
Cooper, S.R., Brush, G.S., 1991. Long-term history of Chesapeake Bay anoxia. Science 254, 992–996.
Cornu, S., Breeze, D., Saada, A., Baranger, P., 2003. The influence of pH, electrolyte type, and surface coating on arsenic(V) adsorption onto kaolinites. Soil Sci. Soc. Am. J. 67, 1127–1132.
Cornwell, J.C., Sampou, P.A., 1995. Environmental controls on iron sulfide mineral formation in a coastal plain estuary. In: Vairavamurthy, M.A., Schoonen, M.A.A. (Eds.), Geochemical Transformations of Sedimentary Sulfur. American Chemical Society, Washington, DC, pp. 224–242.
Cruse, A.M., Lyons, T.W., 2004. Trace metal records of regional paleoenvironmental variability in Pennsylvanian (Upper Carboniferous) black shales. Chem. Geol. 206, 319–345.
Cui, M., Johannesson, K.H., 2017. Comparison of tungstate and tetrathiotungstate adsorption onto pyrite. Chem. Geol. 464, 57–68.
Cui, M., Luther III, G.W., Gomes, M., 2021. Cycling of W and Mo species in natural sulfidic waters and their sorption mechanisms on $MnO_2$ and implications for paired W and Mo records as a redox proxy. Geochim. Cosmochim. Acta 295, 24–48.
Cui, M., Mohajerin, T.J., Adebayo, S., Datta, S., Johannesson, K.H., 2020. Investigation of tungstate thiolation reaction kinetics and sedimentary molybdenum/tungsten enrichments: Implication for tungsten speciation in sulfidic waters and possible applications for paleoredox studies. Geochim. Cosmochim. Acta 287, 277–295.
Dellwig, O., Wegwerth, A., Schnetger, B., Schulz, H., Arz, H.W., 2019. Dissimilar behaviors of the geochemical twins W and Mo in hypoxic-euxinic marine basins. Earth-Sci. Rev. 193, 1–23.
Dollhopf, M.E., Nealson, K.H., Simon, D.M., Luther III, G.W., 2000. Kinetics of Fe(III) and Mn(IV) reduction by the Black Sea strain of *Shewanella putrefaciens* using in situ solid state voltammetric Au/Hg electrodes. Mar. Chem. 70, 171–180.
Domenico, P.A., Schwartz, F.W., 1998. Physical and Chemical Hydrogeology. Wiley, New York.
Emerson, S.R., Huested, S.S., 1991. Ocean anoxia and the concentrations of molybdenum and vanadium in seawater. Mar. Chem. 34, 177–196.
Farrell, Ú.C., Samawi, R., Anjanappa, S., Klykov, R., Adeboye, O.O., Agic, H., Ahm, A.C., Boag, T.H., Bowyer, F., Brocks, J.J., 2021. The sedimentary geochemistry and paleoenvironments project. Geobiology 19, 545–556.
Fendorf, S.E., Zasoski, R.J., 1992. Chromium(III) oxidation by δ-$MnO_2$. 1. Characterization. Environ. Sci. Technol. 26, 79–85.
Fike, D.A., Grotzinger, J.P., Pratt, L.M., Summons, R.E., 2006. Oxidation of the Ediacaran ocean. Nature 444, 744–747.
Foster, A.L., Brown Jr, G.E., Parks, G.A., 2003. X-ray absorption fine structure study of As (V) and Se(IV) sorption complexes on hydrous Mn oxides. Geochim. Cosmochim. Acta 67, 1937–1953.
Freundlich, H.M.F., 1906. Zeitschrift fuer Physikalische Chemie, Stoechiometrie und Verwandtschaftslehre. J. Phys. Electrochem. 57, 385–470.
Goldberg, S., Forster, H.S., Heick, E.L., 1993. Boron adsorption mechanisms on oxides, clay minerals, and soils inferred from ionic strength effects. Soil Sci. Soc. Am. J. 57, 704–708.
Gustafsson, J.P., 2019. Vanadium geochemistry in the biogeosphere–speciation, solid-solution interactions, and ecotoxicity. Appl. Geochem. 102, 1–25.
Hao, J., Cleveland, C., Lim, E., Strongin, D.R., Schoonen, M.A.A., 2006. The effect of adsorbed lipid on pyrite oxidation under biotic conditions. Geochem. Trans. 7, 1–9.
Heinrich, E.W., Levinson, A.A., 1955. Studies in the mica group; x-ray data on roscoelite and barium-muscovite. Am. J. Sci. 253, 39–43.
Ho, Y.-S., McKay, G., 1999. Pseudo-second order model for sorption processes. Process Biochem. 34, 451–465.
Huang, C., Hesselbo, S.P., 2014. Pacing of the Toarcian Oceanic Anoxic Event (Early Jurassic) from astronomical correlation of marine sections. Gondw. Res. 25, 1348–1356.
Huang, J.-H., Huang, F., Evans, L., Glasauer, S., 2015. Vanadium: Global (bio) geochemistry. Chem. Geol. 417, 68–89.
Hudson, J.M., MacDonald, D.J., Estes, E.R., Luther III, G.W., 2019. A durable and inexpensive pump profiler to monitor stratified water columns with high vertical resolution. Talanta 199, 415–424.
Huerta-Diaz, M.A., Morse, J.W., 1990. A quantitative method for determination of trace metal concentrations in sedimentary pyrite. Mar. Chem. 29, 119–144.
Huerta-Diaz, M.A., Morse, J.W., 1992. Pyritization of trace metals in anoxic marine sediments. Geochim. Cosmochim. Acta 56, 2681–2702.
Jeandel, C., Caisso, M., Minster, J.F., 1987. Vanadium behaviour in the global ocean and in the Mediterranean Sea. Mar. Chem. 21, 51–74.
Johannesson, K.H., Tang, J., Daniels, J.M., Bounds, W.J., Burdige, D.J., 2004. Rare earth element concentrations and speciation in organic-rich blackwaters of the Great Dismal Swamp, Virginia, USA. Chem. Geol. 209, 271–294.
Johannesson, K.H., Dave, H.B., Mohajerin, T.J., Datta, S., 2013. Controls on tungsten concentrations in groundwater flow systems: The role of adsorption, aquifer sediment Fe(III) oxide/oxyhydroxide content, and thiotungstate formation. Chem. Geol. 351, 76–94.
Johannesson, K.H., Palmore, C.D., Fackrell, J., Prouty, N.G., Swarzenski, P.W., Chevis, D. A., Telfeyan, K., White, C.D., Burdige, D.J., 2017. Rare earth element behavior during groundwater–seawater mixing along the Kona Coast of Hawaii. Geochim. Cosmochim. Acta 198, 229–258.
Johnson, J.E., Webb, S.M., Thomas, K., Ono, S., Kirschvink, J.L., Fischer, W.W., 2013. Manganese-oxidizing photosynthesis before the rise of cyanobacteria. Proc. Natl. Acad. Sci. 110, 11238–11243.
Jones, C., Crowe, S.A., 2013. No evidence for manganese-oxidizing photosynthesis. Proc. Natl. Acad. Sci. 110, E4118–E.
Konovalov, S.K., Luther, G.W., Friederich, G.E., Nuzzio, D.B., Tebo, B.M., Murray, J.W., Oguz, T., Glazer, B., Trouwborst, R.E., Clement, B., Murray, K.J., Romanov, A.S., 2003. Lateral injection of oxygen with the Bosporus plume-fingers of oxidizing potential in the Black Sea. Limnol. Oceanogr. 48, 2369–2376.
Kunzmann, M., Bui, T.H., Crockford, P.W., Halverson, G.P., Scott, C., Lyons, T.W., Wing, B.A., 2017. Bacterial sulfur disproportionation constrains timing of Neoproterozoic oxygenation. Geology 45, 207–210.
Lagergren, S.K., 1898. About the theory of so-called adsorption of soluble substances. Sven. Vetenskapsakad. Handingarl 24, 1–39.
Langmuir, I., 1918. The adsorption of gases on plane surfaces of glass, mica and platinum. J. Am. Chem. Soc. 40, 1361–1403.

Large, R.R., Halpin, J.A., Danyushevsky, L.V., Maslennikov, V.V., Bull, S.W., Long, J.A., Gregory, D.D., Lounejeva, E., Lyons, T.W., Sack, P.J., 2014. Trace element content of sedimentary pyrite as a new proxy for deep-time ocean–atmosphere evolution. Earth Planet. Sci. Lett. 389, 209–220.
Larsson, M.A., Hadialhejazi, G., Gustafsson, J.P., 2017a. Vanadium sorption by mineral soils: Development of a predictive model. Chemosphere 168, 925–932.
Larsson, M.A., Persson, I., Sjöstedt, C., Gustafsson, J.P., 2017b. Vanadate complexation to ferrihydrite: X-ray absorption spectroscopy and CD-MUSIC modelling. Environ. Chem. 14, 141–150.
Leonhard, P., Pepelnik, R., Prange, A., Yamada, N., Yamada, T., 2002. Analysis of diluted sea-water at the ng $L^{-1}$ level using an ICP-MS with an octopole reaction cell. J. Anal. At. Spectrom 17, 189–196.
Li, J., Bai, Y., Bear, K., Joshi, S., Jaisi, D., 2017. Phosphorus availability and turnover in the Chesapeake Bay: Insights from nutrient stoichiometry and phosphate oxygen isotope ratios. J. Geophys. Res. Biogeosciences 122, 811–824.
Li, W., Feng, X., Yan, Y., Sparks, D.L., Phillips, B.L., 2013. Solid-state NMR spectroscopic study of phosphate sorption mechanisms on aluminum (hydr)oxides. Environ. Sci. Technol. 47, 8308–8315.
Lipp, A.G., Shorttle, O., Sperling, E., Brocks, J.J., Cole, D., Crockford, P.W., Del Mouro, L., Dewing, K., Dornbos, S.Q., Emmings, J.F., 2021. The composition and weathering of the continents over geologic time. Geochem. Perspect. Lett. 7, 21–26.
Lüschen, H., 2004. Vergleichende anorganisch-geochemische Untersuchungen an phanerozoischen C org-reichen Sedimenten: ein Beitrag zur Charakterisierung ihrer Fazies.
Luther III, G.W., 2016. Inorganic Chemistry for Geochemistry and Environmental Sciences: Fundamentals and Applications. John Wiley & Sons.
Lyons, T.W., Diamond, C.W., Planavsky, N.J., Reinhard, C.T., Li, C., 2021. Oxygenation, life, and the planetary system during Earth's middle history: An overview. Astrobiology 21, 906–923.
Lyons, T.W., Reinhard, C.T., Planavsky, N.J., 2014. The rise of oxygen in Earth's early ocean and atmosphere. Nature 506, 307–315.
McBride, M.B., 1997. A critique of diffuse double layer models applied to colloid and surface chemistry. Clays Clay Miner. 45, 598–608.
McKenzie, R.M., 1981. The surface charge on manganese dioxides. Soil Res. 19, 41–50.
Meyer, K.M., Kump, L.R., 2008. Oceanic euxinia in Earth history: Causes and consequences. Annu. Rev. Earth Planet. Sci. 36, 251–288.
Meyers, S.R., Siewert, S.E., Singer, B.S., Sageman, B.B., Condon, D.J., Obradovich, J.D., Jicha, B.R., Sawyer, D.A., 2012. Intercalibration of radioisotopic and astrochronologic time scales for the Cenomanian-Turonian boundary interval, Western Interior Basin, USA. Geology 40, 7–10.
Mohajerin, T.J., 2014. Tungsten speciation, mobilization, and sequestration| Thiotungstate stability constants and examination of (thio)tungstate geochemistry in estuarine waters and sediments. Ph.D. Dissertation. Tulane University, New Orleans, LA.
Monteiro, F.M., Pancost, R.D., Ridgwell, A., Donnadieu, Y., 2012. Nutrients as the dominant control on the spread of anoxia and euxinia across the Cenomanian-Turonian oceanic anoxic event (OAE2): Model-data comparison. Paleoceanography 27.
Morford, J.L., Emerson, S., 1999. The geochemistry of redox sensitive trace metals in sediments. Geochim. Cosmochim. Acta 63, 1735–1750.
Morford, J.L., Emerson, S.R., Breckel, E.J., Kim, S.H., 2005. Diagenesis of oxyanions (V, U, Re, and Mo) in pore waters and sediments from a continental margin. Geochim. Cosmochim. Acta 69, 5021–5032.
Müller, A., Glemser, O., Diemann, E., Hofmeister, H., 1969. Übergangsmetallchalkogenverbindungen. Bildung und Zerfall von Chalkogenoanionen der Übergangsmetalle in wäßriger Lösung. Zeitschrift für Anorg. und Allg. Chemie 371, 74–80.
Murray, R.W., Leinen, M., Isern, A., 1993. Biogenic flux of Al to sediment in the central equatorial Pacific Ocean: Evidence for increased productivity during glacial periods. Paleoceanography 8, 651–670.
Narbonne, G.M., Gehling, J.G., 2003. Life after snowball: The oldest complex Ediacaran fossils. Geology 31, 27–30.
O'Loughlin, E.J., Boyanov, M.I., Kemner, K.M., 2021. Reduction of Vanadium(V) by Iron (II)-Bearing Minerals. Minerals 11, 316.
Oldham, V.E., Owings, S.M., Jones, M.R., Tebo, B.M., Luther III, G.W., 2015. Evidence for the presence of strong Mn(III)-binding ligands in the water column of the Chesapeake Bay. Mar. Chem. 171, 58–66.
Oldham, V.E., Jones, M.R., Tebo, B.M., Luther III, G.W., 2017. Oxidative and reductive processes contributing to manganese cycling at oxic-anoxic interfaces. Mar. Chem. 195, 122–128.
Olson, L., Quinn, K.A., Siebecker, M.G., Luther III, G.W., Hastings, D., Morford, J.L., 2017. Trace metal diagenesis in sulfidic sediments: Insights from Chesapeake Bay. Chem. Geol. 452, 47–59.
Ortiz-Bernad, I., Anderson, R.T., Vrionis, H.A., Lovley, D.R., 2004. Vanadium respiration by Geobacter metallireducens: Novel strategy for in situ removal of vanadium from groundwater. Appl. Environ. Microbiol. 70, 3091–3095.
Owens, J.D., Lyons, T.W., Li, X., Macleod, K.G., Gordon, G., Kuypers, M.M.M., Anbar, A., Kuhnt, W., Severmann, S., 2012. Iron isotope and trace metal records of iron cycling in the proto-North Atlantic during the Cenomanian-Turonian Oceanic Anoxic event (OAE-2). Paleoceanography 27.
Parfitt, G.D., Rochester, C.H., 1983. Adsorption from Solution at the Solid/Liquid Interface. Academic Press, London.
Peacock, C.L., Sherman, D.M., 2004. Vanadium(V) adsorption onto goethite (α-FeOOH) at pH 1.5 to 12: A surface complexation model based on ab initio molecular geometries and EXAFS spectroscopy. Geochim. Cosmochim. Acta 68, 1723–1733.
Pearson, R.G., 1988. Absolute electronegativity and hardness: Application to inorganic chemistry. Inorg. Chem. 27, 734–740.
Piper, D.Z., Dean, W.E., 2002. Trace-element deposition in the Cariaco Basin, Venezuela Shelf, under sulfate-reducing conditions: A history of the local hydrography and global climate, 20 ka to the present. US Geol. Surv.
Ranade, A.C., Müller, A., Diemann, E., 1970. Übergangsmetallchalkogenverbindungen. Evidence for the existence of new Thioanions of Vanadium and Rhenium by their electronic spectra. Zeitschrift für Anorg. und Allg. Chemie 373, 258–264.
Ranjan, D., Talat, M., Hasan, S.H., 2009. Biosorption of arsenic from aqueous solution using agricultural residue 'rice polish'. J. Hazard. Mater. 166, 1050–1059.
Reckhardt, A., Beck, M., Greskowiak, J., Schnetger, B., Böttcher, M.E., Gehre, M., Brumsack, H.-J., 2017. Cycling of redox-sensitive elements in a sandy subterranean estuary of the southern North Sea. Mar. Chem. 188, 6–17.
Rickard, D., 2012. Sulfidic Sediments and Sedimentary Rocks. Elsevier.
Roden, E.E., Tuttle, J.H., 1992. Sulfide release from estuarine sediments underlying anoxic bottom water. Limnol. Oceanogr. 37, 725–738.
Roman, M.R., Brandt, S.B., Houde, E.D., Pierson, J.J., 2019. Interactive effects of hypoxia and temperature on coastal pelagic zooplankton and fish. Front. Mar. Sci. 6, 139.
Sahoo, S.K., 2015. Ediacaran ocean redox evolution. PhD Thesis. University of Nevada, Las Vegas, NV, USA.
Sahoo, S.K., Planavsky, N.J., Kendall, B., Wang, X., Shi, X., Scott, C., Anbar, A.D., Lyons, T.W., Jiang, G., 2012. Ocean oxygenation in the wake of the Marinoan glaciation. Nature 489, 546–549.
Schlesinger, W.H., Klein, E.M., Vengosh, A., 2017. Global biogeochemical cycle of vanadium. Proc. Natl. Acad. Sci. 114, E11092–E11100.
Scholz, F., 2018. Identifying oxygen minimum zone-type biogeochemical cycling in Earth history using inorganic geochemical proxies. Earth-Sci. Rev. 184, 29–45.
Scholz, F., Hensen, C., Noffke, A., Rohde, A., Liebetrau, V., Wallmann, K., 2011. Early diagenesis of redox-sensitive trace metals in the Peru upwelling area–response to ENSO-related oxygen fluctuations in the water column. Geochim. Cosmochim. Acta 75, 7257–7276.
Scott, C., Lyons, T.W., Bekker, A., Shen, Y., Poulton, S.W., Chu, X., Anbar, A.D., 2008. Tracing the stepwise oxygenation of the Proterozoic ocean. Nature 452, 456–459.
Scott, C., Slack, J.F., Kelley, K.D., 2017. The hyper-enrichment of V and Zn in black shales of the Late Devonian-Early Mississippian Bakken Formation (USA). Chem. Geol. 452, 24–33.
Seader, J.D., Henley, E.J., Roper, D.K., 1998. Separation Process Principles. Wiley, New York, USA.
Sell, B., Ovtcharova, M., Guex, J., Bartolini, A., Jourdan, F., Spangenberg, J.E., Vicente, J.-C., Schaltegger, U., 2014. Evaluating the temporal link between the Karoo LIP and climatic–biologic events of the Toarcian Stage with high-precision U-Pb geochronology. Earth Planet. Sci. Lett. 408, 48–56.
Shaw, T.J., Sholkovitz, E.R., Klinkhammer, G., 1994. Redox dynamics in the Chesapeake Bay: The effect on sediment/water uranium exchange. Geochim. Cosmochim. Acta 58, 2985–2995.
Shiller, A.M., Mao, L., 1999. Dissolved vanadium on the Louisiana Shelf: Effect of oxygen depletion. Cont. Shelf Res. 19, 1007–1020.
Sperling, E.A., Wolock, C.J., Morgan, A.S., Gill, B.C., Kunzmann, M., Halverson, G.P., Macdonald, F.A., Knoll, A.H., Johnston, D.T., 2015. Statistical analysis of iron geochemical data suggests limited late Proterozoic oxygenation. Nature 523, 451–454.
Tebo, B.M., Rosson, R.A., Nealson, K.H., 1991. Potential for manganese(II) oxidation and manganese(IV) reduction to co-occur in the suboxic zone of the Black Sea. In: Black Sea Oceanography. Springer, pp. 173–185.
Tribovillard, N., Trentesaux, A., Ramdani, A., Baudinet, F., Riboulleau, A., 2004. Controls on organic accumulation in late Jurassic shales of northwestern Europe as inferred from trace-metal geochemistry. Bull. la Société géologique Fr. 175, 491–506.
Tribovillard, N., Algeo, T.J., Lyons, T., Riboulleau, A., 2006. Trace metals as paleoredox and paleoproductivity proxies: An update. Chem. Geol. 232, 12–32.
Trouwborst, R.E., Clement, B.G., Tebo, B.M., Glazer, B.T., Luther, G.W., 2006. Soluble Mn(III) in suboxic zones. Science 313, 1955–1957.
Vessey, C.J., Lindsay, M.B.J., 2020. Aqueous vanadate removal by iron(II)-bearing phases under anoxic conditions. Environ. Sci. Tech. 54, 4006–4015.
Wainipee, W., Cuadros, J., Sephton, M.A., Unsworth, C., Gill, M.G., Strekopytov, S., Weiss, D.J., 2013. The effects of oil on As(V) adsorption on illite, kaolinite, montmorillonite and chlorite. Geochim. Cosmochim. Acta 121, 487–502.
Wanty, R.B., Goldhaber, M.B., 1992. Thermodynamics and kinetics of reactions involving vanadium in natural systems: Accumulation of vanadium in sedimentary rocks. Geochim. Cosmochim. Acta 56, 1471–1483.
Weber, W.J., Morris, J.C., 1963. Kinetics of adsorption on carbon from solution. J. Sanit. Eng. Div. 89, 31–60.
Wehrli, B., Stumm, W., 1989. Vanadyl in natural waters: Adsorption and hydrolysis promote oxygenation. Geochim. Cosmochim. Acta 53, 69–77.
White, A.F., Peterson, M.L., 1996. Reduction of aqueous transition metal species on the surfaces of Fe(II)-containing oxides. Geochim. Cosmochim. Acta 60, 3799–3814.
Whitmore, L.M., Morton, P.L., Twining, B.S., Shiller, A.M., 2019. Vanadium cycling in the Western Arctic Ocean is influenced by shelf-basin connectivity. Mar. Chem. 216, 103701.
Widler, A.M., Seward, T.M., 2002. The adsorption of gold(I) hydrosulphide complexes by iron sulphide surfaces. Geochim. Cosmochim. Acta 66, 383–402.
Wolfe, A.L., Liu, R., Stewart, B.W., Capo, R.C., Dzombak, D.A., 2007. A method for generating uniform size-segregated pyrite particle fractions. Geochem. Trans. 8, 1–8.
Wong, J., Lytle, F.W., Messmer, R.P., Maylotte, D.H., 1984. K-edge absorption spectra of selected vanadium compounds. Phys. Rev. B 30, 5596.

Wu, F.-C., Tseng, R.-L., Juang, R.-S., 2001. Kinetic modeling of liquid-phase adsorption of reactive dyes and metal ions on chitosan. Water Res. 35, 613–618.
Yang, N., Welch, K.A., Mohajerin, T.J., Telfeyan, K., Chevis, D.A., Grimm, D.A., Lyons, W.B., White, C.D., Johannesson, K.H., 2015. Comparison of arsenic and molybdenum geochemistry in meromictic lakes of the McMurdo Dry Valleys, Antarctica: Implications for oxyanion-forming trace element behavior in permanently stratified lakes. Chem. Geol. 404, 110–125.
Yuan, X., Chen, Z., Xiao, S., Zhou, C., Hua, H., 2011. An early Ediacaran assemblage of macroscopic and morphologically differentiated eukaryotes. Nature 470, 390–393.
Zhu, C., Anderson, G., 2002. Environmental Applications of Geochemical Modeling. Cambridge University Press.
Zhu, H., Xiao, X., Guo, Z., Han, X., Liang, Y., Zhang, Y., Zhou, C., 2018. Adsorption of vanadium (V) on natural kaolinite and montmorillonite: Characteristics and mechanism. Appl. Clay Sci. 161, 310–316.